Pharmacological Research 225 (2026) 108150

Contents lists available at ScienceDirect

Pharmacological Research

journal homepage: www.elsevier.com/locate/yphrs

Tumor-specific targeting of a mitochondrial Kv1.3 channel inhibitor through conjugation to gastrin/cholecystokinin B receptor ligand strongly reduces pancreatic ductal adenocarcinoma in orthotopic models

Sofia Parrasia [a,1], Carlotta Paoli [a,1], Tatiana Varanita [a], Valentina Brillo [a], Mostafa A.L. Abdel-Salam [a,2], Alberto Ongaro [b], Claudia Honisch [c], Beatrice Angi [a], Magdalena Bachmann [a,3], Filippo Bergamin [b], Vincenzo Corbo [d], Elena Fiorini [d], Andrea Rossa [b], Giovanna Bossio [c], Erich Gulbins [e], Alessandro Carrer [a,f], Mario Zoratti [g], Andrea Mattarei [b], Paolo Ruzza [c], Lucia Biasutto [g,*], Ildiko Szabo [a,*]

[a] Department of Biology, University of Padova, Italy
[b] Department of Pharmaceutical and Pharmacological Sciences, University of Padova, Italy
[c] CNR Institute of Biomolecular Chemistry, Padova, Italy
[d] Department of Engineering for Innovation Medicine, University of Verona, Italy
[e] Department of Molecular Biology, University of Essen, Germany
[f] Veneto Institute of Molecular Medicine (VIMM), Padova, Italy
[g] CNR Institute of Neuroscience, Padova, Italy

ARTICLE INFO

Keywords:
Mitochondria
Kv1.3 channel
Pancreatic cancer
Tumor-targeting peptides

ABSTRACT

Pancreatic ductal adenocarcinoma (PDAC) is a highly chemoresistant and immunoresistant tumor with an overall five-year survival rate of less than 10 %. Current treatments for PDAC are rather limited, highlighting the importance of finding novel strategies. In this study, we investigated a strategy for the tumor-specific targeting of PAPTP, a small molecule that reduces PDAC growth by inhibiting the mitochondrial potassium channel mtKv1.3, thereby inducing mitochondrial dysfunction and killing cancer cells. PAPTP was reversibly conjugated to three tumor-penetrating peptides: iRGD, VH434, and a short version of minigastrin (CCK2p). These recognize neuropilin-1 and integrin (iRGD), the low-density lipoprotein receptor (VH434), and the gastrin/cholecystokinin B receptor (CCK2p). *In vivo* pharmacokinetic studies revealed that the PAPTP-bound iRGD peptide underwent rapid metabolic cleavage, which prevented optimal uptake of the construct into PDAC. The VH434 conjugate was highly hemolytic. However, CCK2p-PAPTP exhibited preferential distribution to the pancreas in animals bearing orthotopic PDAC. Efficacy studies revealed a reduction in mean tumor volume of up to 65 % in two independent orthotopic mouse models, with no tumor evident in some of the animals treated with the CCK2p-bound PAPTP construct. Our data suggest that tumor-specific targeting of small molecules may be a promising strategy for precision medicine against PDAC.

1. Introduction

The incidence of pancreatic ductal adenocarcinoma (PDAC), a cancer with a poor prognosis and an astonishingly low survival rate, is rising worldwide and among all age groups [1,2]. Therapeutic options for patients with metastatic disease only offer modest survival benefits as PDAC is resistant to both conventional and immune-based therapies [3]. PDAC is characterized by a high heterogeneity [4] and an acidic tumor microenvironment [5]. PDAC is generally caused by multiple mutations of poorly druggable oncogenes, most frequently KRAS, P53, CDKN2A

* Corresponding authors.
E-mail addresses: lucia.biasutto@cnr.it (L. Biasutto), ildiko.szabo@unipd.it (I. Szabo).
[1] Shared first authorship.
[2] Present address: UPMC Hillman Cancer Center, Pittsburgh, PA, USA
[3] Present address: Dana Farber Cancer Institute, Boston, MA, USA.

https://doi.org/10.1016/j.phrs.2026.108150
Received 31 August 2025; Received in revised form 18 February 2026; Accepted 19 February 2026
Available online 20 February 2026
1043-6618/© 2026 The Authors. Published by Elsevier Ltd. This is an open access article under the CC BY license (http://creativecommons.org/licenses/by/4.0/).

and SMAD4. A dense immunosuppressive stroma, which may account for up to 80 % of the tumor mass and a brisk tumor microenvironment (TME) constitute a tight barrier that prevents drugs from reaching tumor cells efficiently and contribute to PDAC's refractoriness to currently available therapies by preventing efficient drug delivery to tumor cells [6]. In addition to the aforementioned oncogenic mutations, constitutive phosphorylation (at Tyr705) of the Signal Transducer and Activator of Transcription-3 (STAT3) leads to its aberrant activation. STAT3 may be more important than oncogenic KRAS in PDAC, as it is a major factor in tumor growth, stromal modification, gemcitabine (2′,2′-difluoro-2′-deoxycytidine; dFdC) resistance and repression of the anti-cancer immune response [7]. Importantly, inhibition of STAT3 results in stroma remodeling and improved drug delivery [8].

We have recently demonstrated that PAPTP, a small molecule that targets the mitochondrial Kv1.3 potassium channel, can decrease STAT3 phosphorylation in PDAC cells [9]. Potassium channels, including Kv1.3 are promising pharmacological targets in oncology [10–13], also in the context of PDAC [14–17]. PAPTP can reach tumor cells and reduce PDAC growth, as demonstrated in SCID models using Colo357 human cells harboring KRAS and p53 mutations [18], immunocompetent PDAC orthotopic mouse models [19,20] and metastatic pancreas cancer [21]. In the latter two studies we used mouse Pan02 cells characterized by SMAD4 mutation [22] or the KPC mouse PDAC line with p53 and KRAS mutations [23], respectively. Importantly, no signs of toxicity were observed in the *in vivo* experiments upon treatment with 5nmol/gbw [18].

PAPTP specifically targets the mitochondrial potassium channel mtKv1.3, which is highly expressed in human PDAC [19,24], via a positively charged triphenylphosphonium group that is attached to the specific Kv1.3 inhibitor PAP-1 [25]. PAPTP selectively kills cancer cells *in vivo*, through a reactive oxygen species (ROS)-mediated cell death involving respiratory chain complex I [18,26–28]. Importantly, this drug exhibits selectivity towards cancer cells for two reasons: i) it accumulates preferentially in the mitochondria of cancer cells, which have a hyperpolarised membrane potential compared to the mitochondria of healthy cells; and ii) it acts preferentially in cancer cells that overexpress Kv1.3 compared to healthy cells. However, PAPTP is unable to eradicate PDAC when applied alone, despite its ability to kill almost completely all tested PDAC lines *in vitro*. In principle, one way to further enhance the *in vivo* effects of our drug without inducing any toxicity is to allow it to accumulate selectively in tumor tissue. One of the most promising pharmacological tools to achieve this goal is the use of peptides as target-recognition tools (for reviews see e.g. [29–31]).

In the field of oncology, peptides that target tumor cells or the tumor vasculature have demonstrated significant potential. Both cancer cells and tumor vasculature express a number of specific markers and those related to angiogenesis can therefore be targeted while sparing healthy cells and normal blood vessels. We have recently synthesized three conjugates of PAPTP to the A7R peptide, which binds to both neuropilin-1 (NRP-1) and vascular endothelial growth factor receptor-2 (VEGFR2/KDR) (B1), disrupting their receptor-coreceptor interaction and reducing angiogenesis and tumor growth. Two of the three constructs however induced hemolysis. The third, designated PAPTP-I-DA7R, exhibited suboptimal physico-chemical properties, thereby hindering its applicability *in vivo* [32].

The present study investigated the potential for conjugation of PAPTP with three other tumor-penetrating and tumor-targeting peptides, which target epitopes that characterize PDAC cancerous cells or the tumoral neovasculature. One such peptide that has been exploited to successfully target mouse PDAC tissue and enhance the effect of gemcitabine and gemcitabine + nab-paclitaxel upon co-injection [33], is the cyclic, tumor-penetrating, internalizing RGD (iRGD) peptide (CRGD[K/R]GP[D/E]C) [34,35]. This co-treatment has recently entered Phase 1 clinical trials revealing acceptable toxicity in metastatic PDAC patients [36]. Furthermore, the concomitant administration of iRGD has been shown to enhance the uptake and efficacy of an irinotecan-loaded silicasome carrier in vivo [37], even in cases of desmoplastic PDAC. The remarkable tumor-homing activity of iRGD is associated with the significant expression of specific integrins, namely αvβ3 and αvβ5 (a receptor for fibronectin), and potentially αvβ6, on cancer cells [38]. Specifically, the expression of β5 integrin in tumor cells is a prerequisite for the tumor-penetrating activities of iRGD [33]. Following binding to integrins through the RGD motif, the peptide is cleaved by proteases to produce a CRGDK/R fragment, which contains a "C-end Rule" (CendR) motif: (R/K) XX(R/K). The CendR motif has been demonstrated to bind to Neuropilin-1 (NRP-1), a tyrosine kinase coreceptor that plays a role in invasion, migration and angiogenesis. The CendR–NRP-1 interaction enhances vascular transcytosis and permeability, thereby facilitating the delivery of chemotherapeutic agents co-injected with iRGD to tumor cells. It is important to note that the CendR motif also functions as a cell-penetrating peptide, undergoing transcytosis and enhancing the delivery of conjugated drugs to tumor cells. However, to the best of our knowledge, studies to date have focused on coadministration rather than on iRGD-drug conjugates in the case of PDAC.

The second tumor-homing peptide under consideration is VH434 (CMPRLRGC), which was identified by screening complex phage-display peptide libraries on the human low-density lipoprotein receptor (LDLR). This peptide specifically and non-competitively binds to human and rodent LDLRs [39,40]. It has been established that following cargo binding, LDLR is internalized by endocytosis and then recycled to the cell surface following cargo release [41]. Notably, LDLR is highly expressed in pancreatic cancers including KIC mice (LSL-$Kras^{G12D}$; $Ink4a/Arf^{fl/fl}$; Pdx1-^{Cre}) [42] and $Kras^{LSL.G12D/+}$; Pdx1^{-Cre} (KC) as well as $Kras^{LSL.G12D/+}$; $Trp53^{R172H/+}$; Pdx1^{-Cre} (KPC) models [43,44], where it is considered to act as metabolic driver of the disease progression. Consistently, a fluorescent conjugate comprising an LDLR-targeting peptide effectively and specifically recognized PDAC tumoral and metastatic tissues [45]. While PDAC-specific targeting with a high efficacy was demonstrated, no chemotherapeutic agents were employed.

A further targeting peptide that holds great promise for the treatment of PDAC is minigastrin, a ligand that targets the gastrin/cholecystokinin-2 (CCK2) receptors [46]. CCK2R (also known as CCKBR or gastrin receptor), is expressed in the brain, stomach, pancreas, and gallbladder. In contrast to CCK1R, CCK2R demonstrates a high affinity for gastrin. The progression of PDAC is facilitated by the CCK2R receptor type; consequently, a clinical trial employing a CCK1R antagonist proved unsuccessful [47]. Human gastrin is a peptide composed of 34 amino acids. In addition, it exists in several C-terminal truncated forms, including minigastrin, a 13-residue peptide with the sequence LEEEEEAYGWMDF-NH_2 [46]. This comprises the Glu-Ala-Tyr-Gly-Trp-Met-Asp-Phe (EAYGWMDF) sequence (named CCK2p here) used in our study. The rationale for using the shortened version of minigastrin lays in the observation that minigastrin lacking LEEEE at the N-terminus showed the best pharmacokinetic properties, with the highest tumor/kidney ratio and low uptake by nontarget tissues and recognizes CCK2R (CCKBR) with high affinity, in the nM range [48,49]. The CCK2R pathway is a key driver of pancreatic tumorigenesis [50]. Gastrin is expressed exclusively during development; however, it is re-expressed in pancreatic intraepithelial neoplasias (PanINs) and in human pancreatic cancer, as well as in the human pancreatic cancer cell line (e.g. PANC-1). In addition, CCK2R was identified in a Pdx1^{-Cre}/LSL-$Kras^{G12D}$ transgenic mouse model of PDAC. The progression of precancerous pancreatic lesions was halted by the blockade of CCK2R with proglumide in this model [51] and CCK2R antagonists netazepide and JNJ-26070109 exerted a strong inhibitory effect on the incidence of PDAC in $p48^{Cre/+}$-LSL-$Kras^{G12D}$ model [52].

In the present study we synthesized and characterized PAPTP fused to iRGD, VH434 and the short version of minigastrin, CCK2p. We show that fusion of PAPTP to iRGD renders the tumor-targeting peptide highly susceptible to excessive hydrolysis, thereby preventing its efficacious action *in vivo*. The VH434 construct proved hemolytic. On the other hand, CCK2p fused to PAPTP demonstrated targeted delivery to PDAC

and a reduction in tumor size in two distinct orthotopic models.

2. Results

2.1. The receptors for tumor-targeting peptides are highly expressed in human and mouse PDAC samples

As a first step, we interrogated the publicly available TCGA database in order to further confirm our own data and data from literature showing an enhanced expression of KCNA3 encoding Kv1.3, the target of PAPTP, as well as of the proteins recognized by the specific peptides. In accordance with our previous results on a small cohort of PDAC patients with resectable tumor mass, expression of KCNA3 in the TCGA Pan-Cancer database shows a significantly higher expression level of the channel-coding gene in the tumor tissues compared to healthy tissue (Fig. 1A), while expression of the regulatory β subunit (KCNAB3) did not change. The expression levels of both integrin αV and integrin β5 are elevated in tumor tissues in comparison to healthy samples, a phenomenon that is analogous to that observed for LDLR and NRP-1. Surprisingly however, while the gastrin level is elevated in the tumor, the expression level of CCK2R was reduced, in a manner analogous to that observed in stomach adenocarcinoma (STAD) (see Figure S1A). In healthy human pancreatic tissue, the expression of CCK2R is found to be at a low level. However, it has been observed that there is a significant increase in the expression of this gene during the development of pancreatic cancer [53]. Later studies highlighted an increased expression of CCK2R in specific pancreatic cancer subtypes [54]. CCK2R was found to be absent in the liver and liver hepatocellular carcinoma (LIHC) (see Figure S1B), as well as in other tissues, including the oesophagus and kidneys (not shown). As illustrated in Fig. 1B, a robust correlation was identified between the tumoral expression levels of some of the examined specific genes and the overall survival of patients. This correlation was particularly evident for KCNAB3, integrin β5 (ITGB5) (part of the heteromeric αvβ5), and LDLR. The Kvβ3 subunits encoded by KCNAB3 have been shown to accelerate the inactivation kinetics of Kv1.3 channels, thereby reducing potassium currents [55]. An interesting observation is the correlation between the expression of KCNA3 and KCNAB3 in healthy pancreas, yet this correlation is absent in pancreatic cancer samples, as illustrated in Figure S1C. Such difference between healthy and pancreatic tumor is true also for another Kv1.3 channel modulator encoded by KCNAB1 (Figure S1D), while it does not occur for KCNAB2 and KCNE4, other regulatory subunits of the channel [55,56] and KCNE4, KCNAB1 and KCNAB2 do not correlate with survival (not shown). These data suggest that PAPTP conjugated with a tumor-targeting peptide may represent a promising strategy against PDAC, given the high tumoral expression levels of KCNA3, NRP-1, ITGAV, ITGB5 and LDLR in humans. Consequently, the focus was directed towards PAPTP-targeting through iRGD and VH434, peptides that exhibit significant conservation across human and murine species, within the preclinical orthotopic mouse model utilizing Pan02 cells.

In order to assess the expression of NRP-1, integrin β5 and LDLR, Pan02 PDAC cells were injected orthotopically into WT mice. Both the non-tumoral (NT) and tumoral (T) tissue pancreas lysates were loaded for each animal. Our results indicated a substantially elevated level of integrin β5 and LDLR expression in tumor tissues in comparison to the healthy tissue derived from the same tumor-bearing mice (see Fig. 1C).

2.2. Synthesis and characterization of PAPTL-TEG-iRGD and PAPTPL-TEG-VH434

In view of the results obtained above, the synthesis of two pro-drugs was carried out. In this process, PAPTP was conjugated with either iRGD or VH434 via a bioreversible linker, thereby enabling the release of the active principle, PAPTPL upon hydrolysis of the reversible linker by endogenous esterases (see Fig. 2A). The workflow of the synthesis and characterization of these constructs is illustrated in Fig. 2B, Pro-drugs are taken up by cancer cells that overexpress specific receptors that recognise peptide ligands, through endocytosis. The pro-drug is then cleaved, allowing the drug to be released into the cytosol and, ultimately, accumulate into the mitochondria in the case of TPP^+ containing compounds such as PAPTPL (Fig. 2C). PAPTPL is the modified version of PAPTP obtained by the addition of a short linker to one of the phenyl rings of the triphenylphosphonium group of PAPTP, in order to permit conjugation with the tumor-targeting peptide in a position presumably not interfering with binding to and inhibition of Kv1.3: the function of this linker is to ensure the stability of the prodrugs, as has been previously observed for other peptide-PAPTP constructs [32,58]. Based on these considerations, the synthesis of iRGD and VH434 was conducted (see Fig. 2D). The targeting peptides were subsequently conjugated to PAPTPL-TEG-N_3, in which the tetraethyleneglycol moiety (TEG) was incorporated to enhance the water solubility of the construct. Please consult the Materials and Methods section, wherein a detailed exposition of the synthesis and physico-chemical characterization of the constructs is provided.

Prior to performing an *in vivo* evaluation of the prodrug distribution, hemolytic activity was assessed. PAPTPL-TEG-VH434 was found to be strongly hemolytic (Fig. 2E), thus leading to its exclusion from further experimentation. Therefore, PAPTPL-TEG-iRGD peptide was subjected to further examination. As previously mentioned, the iRGD cyclic nonapeptide (see Fig. 2D) has been demonstrated to interact with integrin, subsequently undergoing a specific enzymatic cleavage which results in the exposure of a CendR motif. This, in turn, leads to interaction with Neuropilin-1 and internalization in the cell through transcytosis. The tissue distribution of the PAPTPL-TEG-iRGD and the active drug, i.e. PAPTPL, was analyzed following single i.p. administration (5 nmol/gbw conjugate) to C57BL6 mice bearing orthotopic PDAC (Pan02 cells). As it is difficult to achieve the complete and reliable separation of the healthy pancreas from the relatively small tumor for precise quantitative analysis, the whole pancreas (PDAC + healthy tissue) was analyzed by HPLC-UV to quantify the compound, 2 and 6 h after administration. This analysis indicated that at the longer time point, the concentration of PAPTPL-TEG-iRGD decreased to almost zero, while that of PAPTPL increased (Fig. 2F). When considering the full range of species, a time-dependent increase was observed in the pancreas, suggesting that the construct had reached the pancreas but the concentration of the active species, PAPTPL was rather low (Fig. 2F). The predominant circulating species in plasma was the intact derivative, i.e. PAPTPL-TEG-iRGD, indicating the compound's favorable stability in the blood *in vivo* (Fig. 2G). Notably, two smaller cleavage products were also identified (designated PAPTPL-TEG-βAβA(C)), which lost the CendR motif (see Figure S2 for LC-MS identification and structure). 6 h after administration, the concentration of PAPTPL-TEG-iRGD decreased to almost zero, while that of PAPTPL increased (Fig. 2F); PAPTPL-TEG-βAβACRGDR was essentially undetectable in the pancreas, while the quantity of PAPTPL-TEG-βAβA(C) was comparable to that of PAPTPL (Fig. 2G). In all the other analyzed tissues, namely spleen, liver and kidneys, the intact derivative was almost absent/undetectable after 6 h, while the above-mentioned different hydrolytic products were detected (Fig. 2G). The available data provide compelling evidence that the rate of uptake of the prodrug into the pancreas was less rapid than the rate of its metabolic cleavage.

This resulted in the formation of hydrolytic products that lacked the crucial tumor-targeting iRGD and CendR motifs. It has been observed that the process of hydrolysis appears to be particularly advanced in the pancreas in comparison with other tissues, such as the kidneys and the liver (Fig. 2H). This phenomenon may provide a rationale for the limited accumulation of the derivative in the pancreas, given that only PAPTPL-TEG-iRGD and PAPTPL-TEG-CendR are expected to be recognized by integrin and NRP1. It is regrettable that the active PAPTPL concentration released from iRGD-TEG-PAPTPL in the pancreas is rather low and does not reach the EC_{50} value (Fig. 2B). For this reason, we did not proceed with *in vivo* analysis using this PAPTPL-peptide construct.

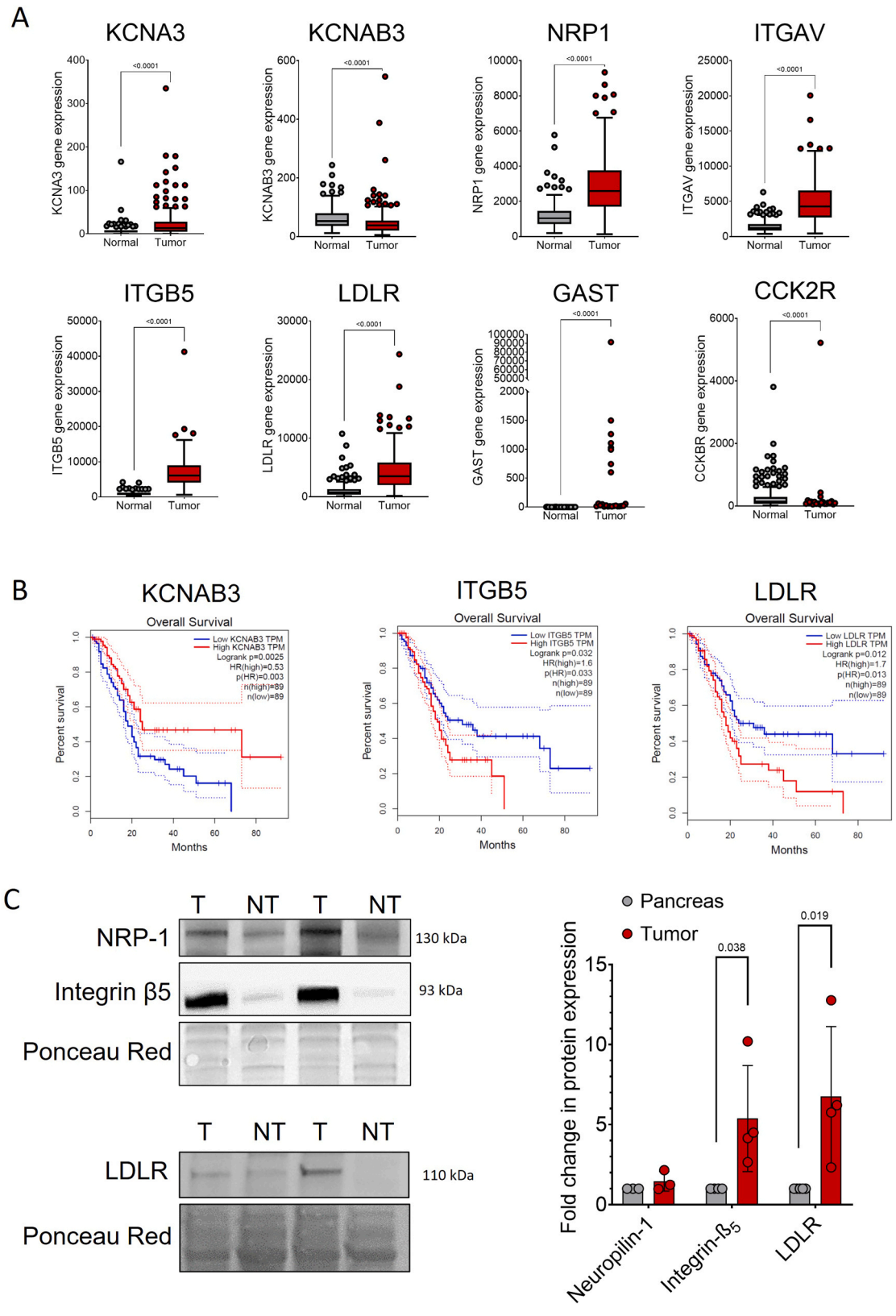


Fig. 1. Expression of receptors for tumor-targeting peptides in human and mouse tumors. Expression of the transcript levels of the indicated genes based on GCD and GTEX datasets. Gray and red columns refer to healthy and tumoral tissues, respectively. Mann-Whitney; significance is shown for each gene. B) Kaplan-Meier analysis of long-term overall survival in relation to the expression of the indicated genes (from GEPIA site). C) Representative Western blots of the indicated proteins from non-tumoral (NT) and tumoral (T) samples from the same animals (n = 2) are shown. Quantification of normalized relative expression (normalization was performed on total proteins stained with Ponceau Red is shown on the right (n = 3 or 4). Western blot analysis on tissue lysates from orthotopic PDAC or from pancreas. Normalization was performed on total proteins stained with Ponceau Red as in [57]. 30 μg/lane of proteins loaded.

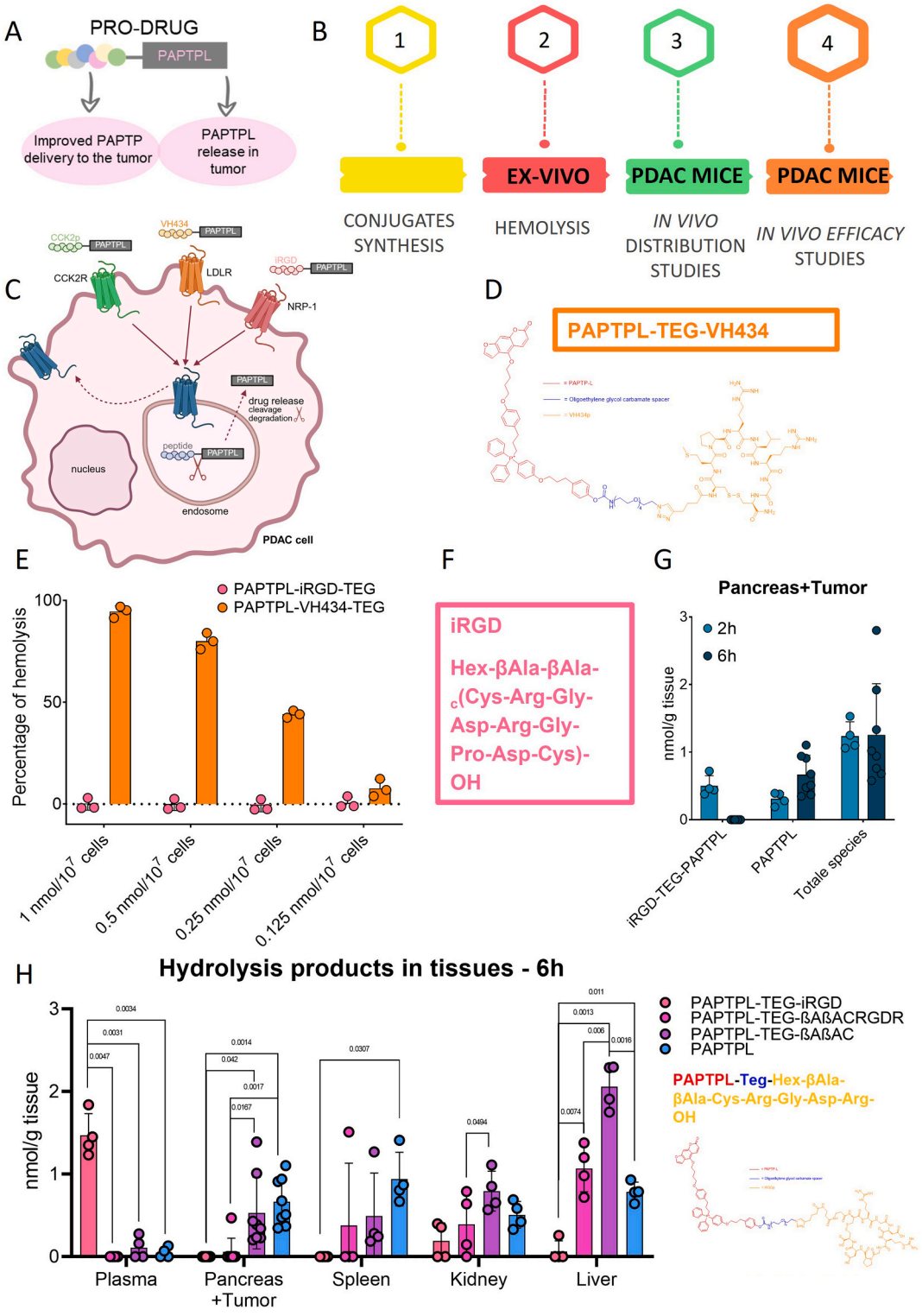


Fig. 2. Characterization of newly synthesized PAPTPL-TEG-iRGD and of PAPTPL-TEG-VH434. A)Scheme of peptide-bound PAPTP as prodrug. B) Workflow of prodrug characterization.C) Schematic representation of prodrugs internalization in the PDAC cells and release into the cytosol. D) Structure of PAPTPL-TEG-VH434 used in this study is shown. E) Hemolytic potential of PAPTPL-TEG-iRGD and PAPTPL-TEG-VH434. Erythrocytes were isolated from fresh mouse blood and incubated with the compounds to be tested. After 15 min, cells were centrifuged and hemoglobin was measured at 450 nm (n = 3). Lysis with Triton X100 and incubation with PBS were used as positive (100 % hemolysis) and negative (0 % hemolysis), respectively. Amounts of the PAPTPL-derivatives are expressed as nmoles/10^7. F) Sequence of the synthesized peptide derivative iRGD (Hex-βAβA-c(CRGDRGPDC); Hex = 5-hexynoic acid. G) Quantification of time-dependent accumulation of PAPTPL-TEG-iRGD and of PAPTPL in the pancreas with Pan02-induced PDAC. PAPTPL-TEG-iRGD was administered by i.p. injection at 5 nmol/gbw. After 2 or 6 h, mice were sacrificed, organs were explanted, immediately frozen in liquid nitrogen and stored at −80°C. The quantification of PAPTPL-TEG-iRGD and its metabolites was performed by HPLC UV. Identification of each metabolite was performed by LC-MS. H) Concentrations of PAPTPL-TEG-iRGD, PAPTPL and intermediate proteolysis products detected in different organs of mice bearing Pan02 orthotopic PDAC, 6 h after i.p. administration of PAPTPL-TEG-iRGD. Two-way Anova; significance is shown. Please consult Fig. S2 for the LC-MS spectra of the metabolites. Inset shows the chemical structure of PAPTPL-TEG-iRGD.

2.3. Characterization of PAPTPL-TEG-CCK2p

As mentioned above, the gastrin receptor (CCK2R) expression significantly increases during the development of pancreatic cancer [53]. Thus, CCK2R is a possible target, also because of its near-absence in other tissues (see Figure S1 and not shown). The present study firstly sought to validate the expression of CCK2R in murine cultured PDAC cells in order to subsequently test the effect of the PAPTPL-TEG-CCK2p construct (Fig. 3**A**). The Western blot shows that both Pan02 and Kras$^{(G12D/+)}$; Trp53$^{(R172H/+)}$; Pdx1^{-Cre} KPCY 2838c3 cells express CCK2R (Fig. 3A). The two CCK2R-specific antibodies employed in this study recognize both human and mouse CCK2R (CCKBR) receptors, but not CCK1R (CCKAR). Next, we sought to demonstrate that PAPTP as well as PAPTPL have similar action in both cell types. As demonstrated in Fig. 3B-E, the incorporation of the linker in PAPTPL exhibited no substantial impact on the IC_{50} of PAPTP, which remained within the micromolar range. In accordance with our preceding findings, which showed that mutant KRAS renders PDAC cells more susceptible to PAPTP [21], the IC_{50} values for both PAPTP and PAPTPL were reduced in comparison to the Pan02 cell line, which lacks a KRAS mutation. Importantly, the same drugs decreased the viability of the 266–6 control pancreatic acinar cell line [59] at substantially higher concentrations, indicating a capacity to selectively kill cancer cells. This is in agreement with our previous results [18]. To prove that PAPTPL and not the CCK2p of the prodrug acted on mitochondria and reduced functionality of this organelle, we examined the effect of the peptide (linked to Fluo, see below) and of PAPTPL separately on the mitochondrial membrane potential, ROS release and mitochondrial network (Fig. 3H-M). The mitochondrial membrane potential decreased significantly following both acute treatment with PAPTPL (Fig. 3H) and incubation of the cells with the whole pro-drug (Fig. 3I). Accordingly, there was an increase in mitochondrial ROS production (Fig. 3J and K). As mentioned in the introduction, PAPTP-triggered loss of the membrane potential is associated with mitochondrial swelling, due to the opening of the permeability transition pore. Here we observed a rapid mitochondrial network fragmentation and swelling upon both acute treatment with PAPTPL and following longer incubation with the pro-drug (a longer time-scale for exerting an effect is expected, since the pro-drug has to be hydrolyzed within the cells in order to release PAPTPL).Overall, these results confirm that PAPTPL can selectively kill cancer cells from two pancreatic ductal adenocarcinoma (PDAC) lines by inducing mitochondrial dysfunction.

Next, we evaluated the expression of CCK2R in various tissues from Pan02-injected mice (Fig. 4A-C). In order to facilitate a more comprehensive evaluation of the differential expression between a healthy pancreas and PDAC, the organs and liver were obtained from healthy animals and from animals bearing Pan02 orthotopic PDAC. Furthermore, the presence of CCK2R was detected, albeit at a lower level, in an intrasplenic injection metastatic model that resulted in liver spread [60]. The data presented herein suggest that Pan02 cell-induced tumors are a suitable model for studying the effect of PAPTPL-TEG-CCK2p, which may be targeted exclusively to PDAC via binding to the CCK2R receptor. CCK2p (Fig. 3A) conjugated with PAPTP and TEG was not hemolytic (Fig. 4D). To investigate the accumulation of the CCK2p-containing construct through fluorescence-based imaging techniques, we synthesized a fluorescent analog of PAPTPL-TEG-CCK2p, namely NBDTP-TEG-CCK2p named Fluo-CCK2p for simplicity, by substituting the PAP-1 drug moiety with the fluorophore 7-nitrobenz-2-oxa-1,3-diazole (NBD). In this construct, a non-bioreversible linker was employed to ensure that the NBD fluorophore remained covalently bound, thereby enabling reliable imaging of probe localization. NBD was selected owing to its favorable photophysical and chemical properties, including strong emission in the visible range, low molecular weight, and lack of ionic functional groups. These features minimize interference with the pharmacodynamic behavior and biodistribution of the labeled conjugate, making NBD a widely used probe in biochemical and chemical biology applications [61].

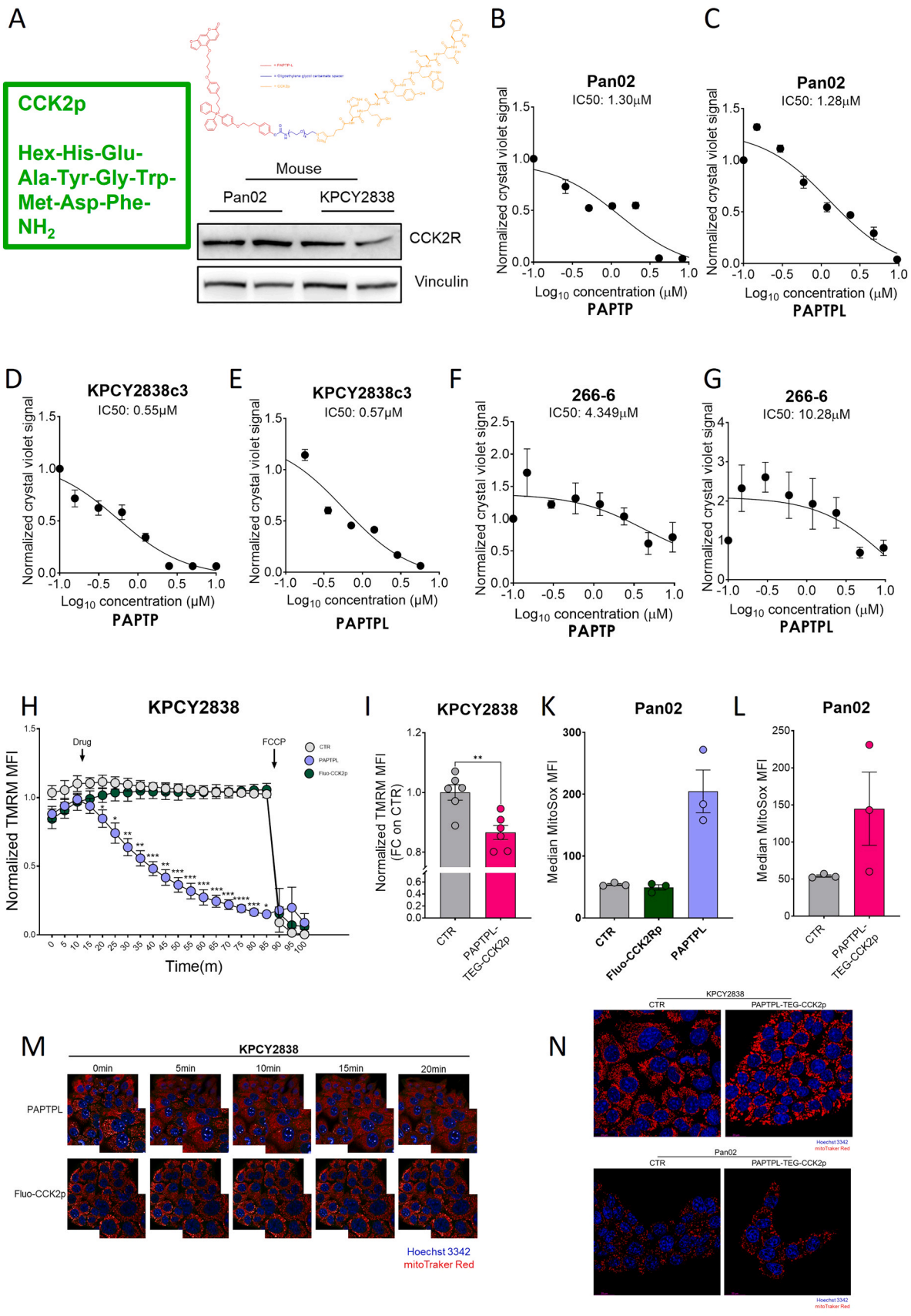
Fluo-CCK2p was effectively absorbed by cultured Pan02 cells, as determined by FACS analysis (Fig. 4E). Furthermore, its presence was observed *in vivo*, six hours after intraperitoneal injection, as illustrated in Fig. 4F. It is noteworthy that the fluorescent signal was exclusively detected in the pancreas, with two out of three mice exhibiting positive signals in the tumor itself, which had been established for 14 days following the injection of Pan02 cells.

The data presented here collectively suggests that CCK2p-linked PAPTP is taken up with efficiency by PDAC. In accordance with this, pharmacokinetic studies in Pan02-induced PDAC-harboring mice highlighted a rapid accumulation up to 170 nmol/g tissue of the total species within 2 h following a single i.p. injection of PAPTPL-TEG-CCK2p in the pancreas+tumor sample, but PAPTPL was present at low quantity, suggesting a slow cleavage of the construct (Fig. 4G). This assumption was confirmed by the observation that the prodrug was present after 6 h following administration, in contrast to the original unmodified drug, PAPTP, whose concentration diminished over time (Fig. 4H). The quantity of the various cleavage products (identified by LC-MS) in different tissues was determined by HPLC-UV analysis, revealing the presence of the prodrug PAPTPL-TEG-CCK2p and of the hydrolytic product PAPTPL-TEG-His almost exclusively in the pancreatic tissue (Fig. 4I), thus further confirming the results shown in Fig. 4F. The mean concentration of the two aforementioned compounds was determined to be 10 nmol/g tissue after a duration of 6 h. The concentration of the final cleavage product, PAPTPL, slightly increased at 14 h with respect to 2 h post-injection (Fig. 4J), further corroborating the hypothesis of a protracted hydrolysis of the prodrug.

2.4. In vivo effects of CCK2p-TEG-PAPTPL in two mouse orthotopic models

The achievement of tumor-specific targeting of the prodrug prompted the investigation of its *in vivo* effects. In the first set of experiments, an orthotopic immunocompetent syngenic mouse model was established using Pan02 cells, as tumors arising from this process have been observed to exhibit desmoplasia which counteracts the fast diffusion of drugs [62]. The treatment was every second day beginning on the 5th day after surgical implantation, with five doses of PAPTP or PAPTPL-TEG-CCK2p (using the same concentration). The animals were euthanized one day after the last injection for further analysis (see Fig. 5A). While PAPTP alone induced a 65 % reduction in tumor volume, the effect of PAPTPL-TEG-CCK2p was comparable and did not enhance the effect of the drug (Fig. 5B). It was demonstrated that both PAPTP and the pro-drug triggered DNA fragmentation to a similar extent, as measured using the TUNEL assay (Fig. 5C). Furthermore, it was observed that there was a reduction in proliferation, as indicated by Ki67 staining (Fig. 5D). Gross histological alterations were not observed in hematoxilin/eosin staining (Fig. 5D).

Next, an orthotopic desmoplastic model was established using Kras$^{(G12D/+)}$; Trp53$^{(R172H/+)}$; Pdx1^{-Cre} KPCY 2838c3 cells which express YFP. These cells have been shown to give rise to T-cell inflamed tumors [63]. These cells expressed CCK2R (see Fig. 6A) and the fluorescent peptide Fluo-CCK2p was efficiently absorbed KPC cells not expressing YFP (see Fig. 6B). *In vivo* experiments performed as illustrated in Fig. 5A demonstrated a mean reduction in tumor volume of 65 % (see Fig. 6C). In this system, the pro-drug treatment was found to be more efficacious than PAPTP alone. Moreover, it is of particular significance that, in two out of eight mice, the tumor was not detectable following treatment. In an effort to correlate this effect with a higher concentration of the total species of the prodrug, the concentration of PAPTP and of CCK2p-TEG-PAPTPL and its cleavage products was measured at the endpoint of the experiment shown in Fig. 6C. This revealed a lower but not statistically significant mean concentration of the prodrug total species in most of the animals compared to PAPTP (Fig. 6D) upon chronic treatment (5 injections on alternate days) and



(caption on next page)

Fig. 3. Mitochondrial effects of newly synthesized PAPTPL-TEG-CCK2p. A) Chemical structure of PAPTPL-TEG-CCK2p and sequence of the synthesized peptide derivative CCK2p (Hex-HEAYGWMDF-NH_2); Hex = 5-hexynoic acid. Representative Western blot analyses of CCK2R protein levels (with an antibody targeting both the highly homologous murine and the human forms of CCK2R (Abcam ab77077) on Pan02 and KPCY2838c3 cells. 25 μg/lane of proteins loaded, vinculin (130 kDA) used as loading control. B-G) Curve fitting and IC_{50} of PAPTP and PAPTPL on (B-C) Pan02, (D-E) KPCY2838, and (F-G) 266–6 cells based on crystal violet staining of the respective cell lines treated with increasing concentration of PAPTP or PAPTPL.H) Mitochondrial membrane potential measurement in KPCY2838 cells after acute treatment with 5 μM of PAPTPL (blue) or Fluo-CCK2p (green). 1 μM of FCCP was used as a positive control for mitochondrial membrane depolarization (n = 3). Dunnett's multiple comparisons test; * $p < 0.05$, ** $p < 0.01$. I) Mitochondrial membrane potential measurement in KPCY2838 cells after overnight treatment with 5 μM of PAPTPL-TEG-CCK2p. Data are shown as Δ between basal measurement and measurement after the addition of 1 μM of FCCP and normalized on the control (n = 6). Mann-Whitney test, **$p < 0.01$. J) MitoSox median fluorescence intensity of Pan02 cells treated with 5 μM of Fluo-CCK2p or PAPTPL for 2 h. K) MitoSox median fluorescence intensity of Pan02 cells treated with 5 μM of PAPTPL-TEG- CCK2p overnight. L) Evaluation of mitochondrial swelling in KPCY2838 cells in response to 5 μM PAPTPL or Fluo-CCK2p at the indicated time frames. Mitochondria are stained in red, nuclei are stained in blue. M) Evaluation of mitochondrial swelling in KPCY2838 and Pan02 cells treated with 5 μM of PAPTL-TEG-CCK2p overnight. Mitochondria are stained in red, nuclei are stained in blue.

measured 6 h following the last injection.

Finally, in light of the promising results above, we tested for the presence of the CCK2R receptor in two human PDAC cell lines. Both lines showed substantial receptor expression (Fig. 6E), suggesting that the strategy described here may have translational potential.

3. Discussion

Ion channels of the plasma membrane and of mitochondria have been identified as promising oncological targets. These channels often exhibit aberrantly high expression in various types of cancer, can be targeted by specific drugs at very low concentrations, and affect a myriad of oncogenic signalling processes [64] and cellular bioenergetics [65]. Kv1.3 is among the most studied ion channels as its pharmacological targeting may affect cancer cells behavior (e.g. [66–68]). We previously developed PAPTP, a mitochondria-targeted, high-affinity, specific Kv1.3 inhibitor. Systemic PAPTP administration to various cancer mouse models did not induce systemic toxicity. Here, we demonstrate that PAPTPL — a modified version of PAPTP, created by adding a short linker to one of the phenyl rings of the triphenylphosphonium group (to enable conjugation with a tumour-targeting peptide) — can effectively induce mitochondrial dysfunction, resulting in a rapid loss of mitochondrial membrane potential and the disruption of the mitochondrial network. This ultimately leads to a significant reduction in cell viability. Importantly, PAPTPL was much less efficient in a control acinar cell line, indicating its selectivity towards cancer cells. However, Kv1.3 is expressed also in the immune cells of the tumor microenvironment [15,69]- Therefore, despite the absence of signs of malaise or toxicity, Kv1.3 modulation at the systemic level may have additional, undesired effects, for example by affecting $CD8^+$ T cell function [70,71], regulatory T cells function [72,73] or tumor-associated macrophage efficacy [74,75].

The objective of the present study was therefore to target one of the promising mitochondrial Kv1.3 inhibitors, PAPTP, to the PDAC tumor in the whole body following intraperitoneal injection. In order to achieve this goal, three distinct tumor-targeting peptides were utilized. Peptide-PAPTP conjugates have small-molecular weight, which may facilitate rapid and profound penetration into tumor tissues. The utilization of a small-sized molecule ensures precise dosage control during administration, a benefit that is facilitated by the known exact molecular weight. In addition, the small MW conjugates are generally not immunogenic. iRGD was selected as the primary agent due to its recognition as an optimal solution for precision targeting of solid tumors, exhibiting unique tumor-penetrating and cell-internalizing properties. iRGD has been utilized as a targeting moiety bound to nanoparticles (e.g. [33,37, 76] for review see e.g. [77]) or fused to small proteins such as interleukin-24 (e.g. [78]). To the best of our knowledge, our study represents one of the few examples where iRGD was conjugated to a small molecule and tested *in vivo* against PDAC. Recently, camptothecin conjugated to iRGD through a linker was administered with positive results in order to reduce colon cancer growth in a xenograft model [79]. TEG was employed in a manner analogous to our own strategy, with the aim of enhancing solubility. However, in contrast to our study, they utilized a stable, covalent linkage between iRGD and camptothecin. It is proposed that non-cleavable crosslinkers can undergo lysosomal breakdown, thereby releasing the cargo. In our study the decision was taken to employ a bioreversible linker strategy, with the objective of preserving the high affinity of binding of PAPTP to mitochondrial Kv1.3. Nevertheless, as demonstrated by the findings presented herein, a non-targeted drug release occurred prior to reaching the destination, owing to an excessive cleavage of the peptide bound to PAPTPL. Specifically, the presence of PAPTP led to the destabilization of the peptide, thereby inducing cleavage that resulted in PAPTPL-Spacer-Cys, which lacked the iRGD sequence. The cyclic nonapeptide which is responsible for carrying the cargo is generally cleaved between the two cysteine residues, as well as the Gly and Lys residues. While these cleavage steps occurred also in our system, an additional, difficult-to-predict hydrolysis took place between Cys and Arg in the Cys-Arg-Gly-Asp sequence. This process resulted in the loss of the Cendr motif (RGD) and prevented optimal accumulation *in vivo* in pancreatic/PDAC tissue only. Further research is necessary to synthesize and evaluate *in vitro* and *in vivo* a version of the PAPTPL-TEG-iRGD construct that exploits non-cleavable crosslinkers, under the assumption that PAPTPL will be released into the cytosol following internalization of the NRP-1-iRGD-TEG-PAPTPL complex.

The strategy employed for iRGD in our study yielded superior results when applied to CCK2p, the short version of minigastrin, given its resistance to PAPTP-triggered degradation. Minigastrin and its derivatives indeed represent promising tumor-targeting peptides [80]. PAPTPL-TEG-CCK2p proved to be more efficient than PAPTP in the KPC orthotopic model compared to the Pan02 model, both characterized by desmoplasia [62]. Conversely, in the Pan02 model PAPTP was slightly better performing than the prodrug. The observed difference is tentatively ascribed to the varying sensitivity of Pan02 and KPC cells to PAPTP; however, the possibility that other factors, including tumor infiltration by immune cells and the level of desmoplasia in the stroma, may also be contributing cannot be excluded. Taking into account the mean values of the quantity of the compounds found in the KPC model pancreatic tissues after chronic treatment (Fig. 5E) and the mean values of tumor volume reduction (Fig. 5D), we estimate that the effectiveness of the prodrug in reducing the tumor volume was approximately 2,7 higher compared to PAPTP (reduction of tumor volume 1.35-fold more effective for the peptide-PAPTPL construct compared to PAPTP; PAPTP concentration is 2-fold higher compared to the total species of the construct). We cannot fully exclude that PAPTP exerts a function *in vivo* also on immune cells of the TME, in addition to PDAC cells, accounting for its high efficiency. However, the hypothesis is rendered unlikely by the observation that $CD4^+$ and $CD8^+$ T lymphocytes and monocytes do not express pharmacologically detectable CCK/gastrin receptors [81]. In contrast, Smith et al. have mentioned that CCK receptors are present in pancreatic epithelial cells, cancer-associated fibroblasts (CAFs), and immune cells. The pharmacological blockade of CCKR receptors (CCK1R and CCK2R) has been shown to enhance the response to immunotherapy in pancreatic cancer [82], although the underlying mechanism and the potential expression of CCK2R in TME immune cells remain to be elucidated. Further research is required to elucidate this aspect and

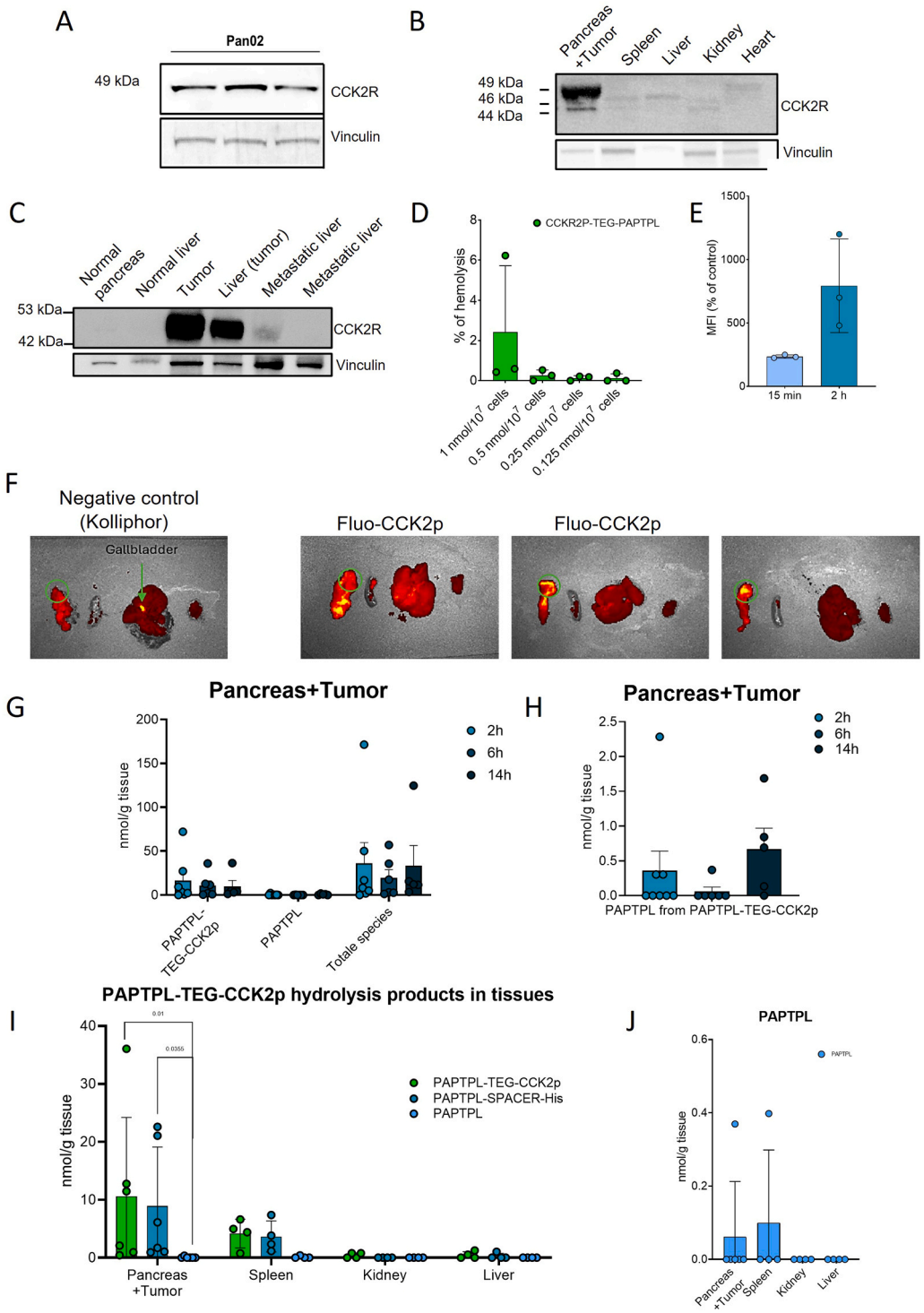


Fig. 4. Characterization of newly synthesized PAPTPL-TEG-CCK2p. A-C) Representative Western blot analyses of CCK2R protein levels (with an antibody targeting the human form of CCK2R) on (A) Pan02 and KPCY2838c3 cells, (B) tissue lysates from orthotopic PDAC (Pan02 cells)-bearing pancreas and normal tissues (liver, spleen, kidney, heart), and (C) tissue lysates of pancreas and liver from healthy controls, orthotopic PDAC (Pan02 cells) and the liver of the same mouse, and metastatic liver obtained by the spleen injection metastatic model. 25 μg/lane of proteins loaded, vinculin (130 kDA) used as loading control. D) Hemolytic potential of PAPTPL-TEG-CCK2p, as in E. E) Time-dependent uptake of 5 μM Fluo-CCK2p into cultured PDAC cells, as assessed by flow cytometry analysis. F) Representative images of tissue distribution (from left to right: pancreas, spleen liver, kidney) of 4 nmol/g fluorescent CCK2p injected i.p. in an orthotopic model of PDAC (grown for 14 days), 6 h following injection. Yellow indicates the fluorescence of Fluo-CCK2p. G) Concentrations of PAPTPL-TEG-CCK2p, PAPTPL and overall amount of PAPTPL-containing species detected in the pancreas with Pan02-induced PDAC, 2, 6 and 14 h after i.p. administration of PAPTPL-TEG-CCK2p. H) Concentrations of the total species of PAPTPL-TEG-CCK2p and of PAPTP alone detected in the pancreas with Pan02-induced PDAC, 2 and hours after i.p. administration of the drugs (enlargement of y-scale; same data as shown in panel H for total species). Each point represent data from a distinct animal. I) Concentrations of PAPTPL-TEG-CCK2p, PAPTPL and intermediate proteolysis products (PAPTPL-TEG-His, here indicated as PAPTPL-SPACER-His) detected in different organs of mice bearing Pan02 orthotopic PDAC, 6 h after i.p. administration of PAPTPL-TEG-CCK2p.Two-way Anova; significance is shown. J) PAPTPL released from PAPTPL-TEG-CCK2p at 2 and 14 h.

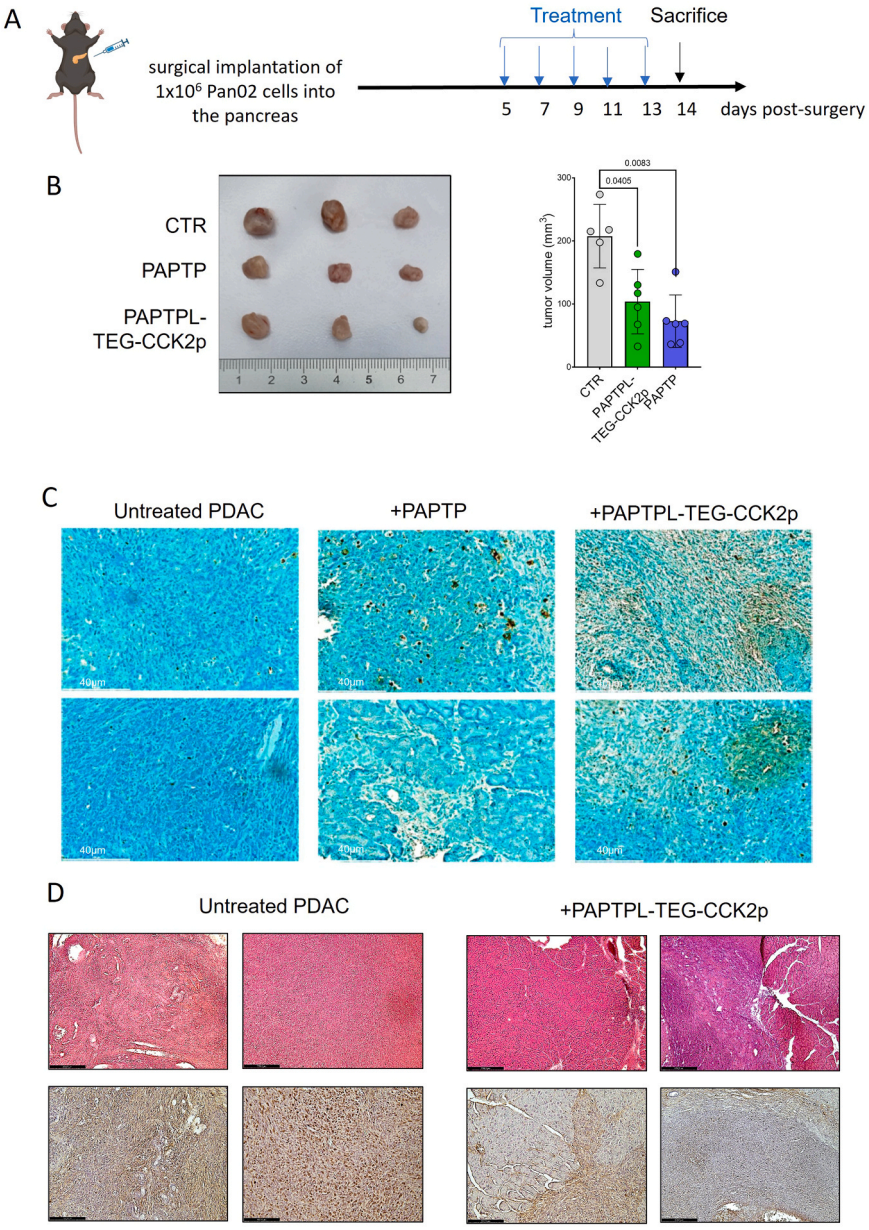


Fig. 5. Tumor volume reduction by CCK2p-TEG-PAPTPL in Pan02 orthotopic model. A) Treatment scheme. B) Representative images of orthotopic PDAC treated with PAPTP or PAPTPL-TEG-CCK2p. Tumors were induced by surgical implantation in the pancreas of 1×10^6 Pan02 cells. The treatment with 5 nmol/gbw of PAPTP (n = 6) or PAPTPL-TEG-CCK2p (n = 6) or vehicle (n = 5) started 5 day after tumor induction, every other day, for a total number of 5 doses. Mice were sacrificed the day after the last dose. Tumor volume (B) calculated as $[hxl^2]/2$. Kruskal-Wallis, significance is shown. C) Tunel immunostain of orthotopic tumors (Pan02 cells) from control, PAPTP treated or PAPTPL-TEG-CCK2p treated mice. Scale bar: 40 μm. Right panel: quantification of the Tunel-positive nuclei. D) Representative images of KI67 and hematoxylin/eosin staining on PDAC tissues from untreated or treated animals as indicated.

ascertain whether the beneficial effects of our construct are also exerted through its action on CAFs and/or immune cells. Notwithstanding, four aspects of the PAPTPL-TEG-CCK2p prodrug are worthy of note: firstly, it accumulated specifically in the pancreas-bearing tumor, with no prodrug detected in the liver or kidneys (Fig. 4F), suggesting that even longer-term treatment would spare these organs from toxicity; secondly, in 25 % of mice, no tumor was found following treatment (Fig. 6 C) (the reasons for the observed variation in response among animals may be attributable to distinct metabolic characteristics and/or varying degrees of desmoplasia); and thirdly, the procedure described here can be exploited in principle for other chemotherapeutic agents as well, and eventually dual-loaded CCK2p can be designed, as with RGD peptides [83]; finally, as shown here, CCKBR expression is maintained after metastatization to liver (Fig. 4C), rendering likely the action of this conjugate not only on the primary tumor, but also on metastatic cells – a hypothesis that remains to be tested.

In murine models, the transgenic expression of the CCKBR in pancreatic acinar cells has been demonstrated to induce increased pancreas growth and transdifferentiation of acinar cells into ductal structures, which in turn leads to the development of pancreatic cancer [84]. As demonstrated by de Weerth and colleagues, the majority of human pancreatic cancer cell lines of ductal origin were found to express CCKB receptor mRNA [85]. ^{111} In-labeled minigastrin has been proposed for the treatment of human colorectal and pancreatic tumors [86]. Indeed, human PANC-1 cells, which were derived from a patient with PDAC and expressed CCK2R, efficiently bound CCK2R-specific DNA aptamers in both *in vitro* and in an orthotopic model [87]. Another study showed that downregulation of CCK2R by siRNA in human AsPC-1, MIA

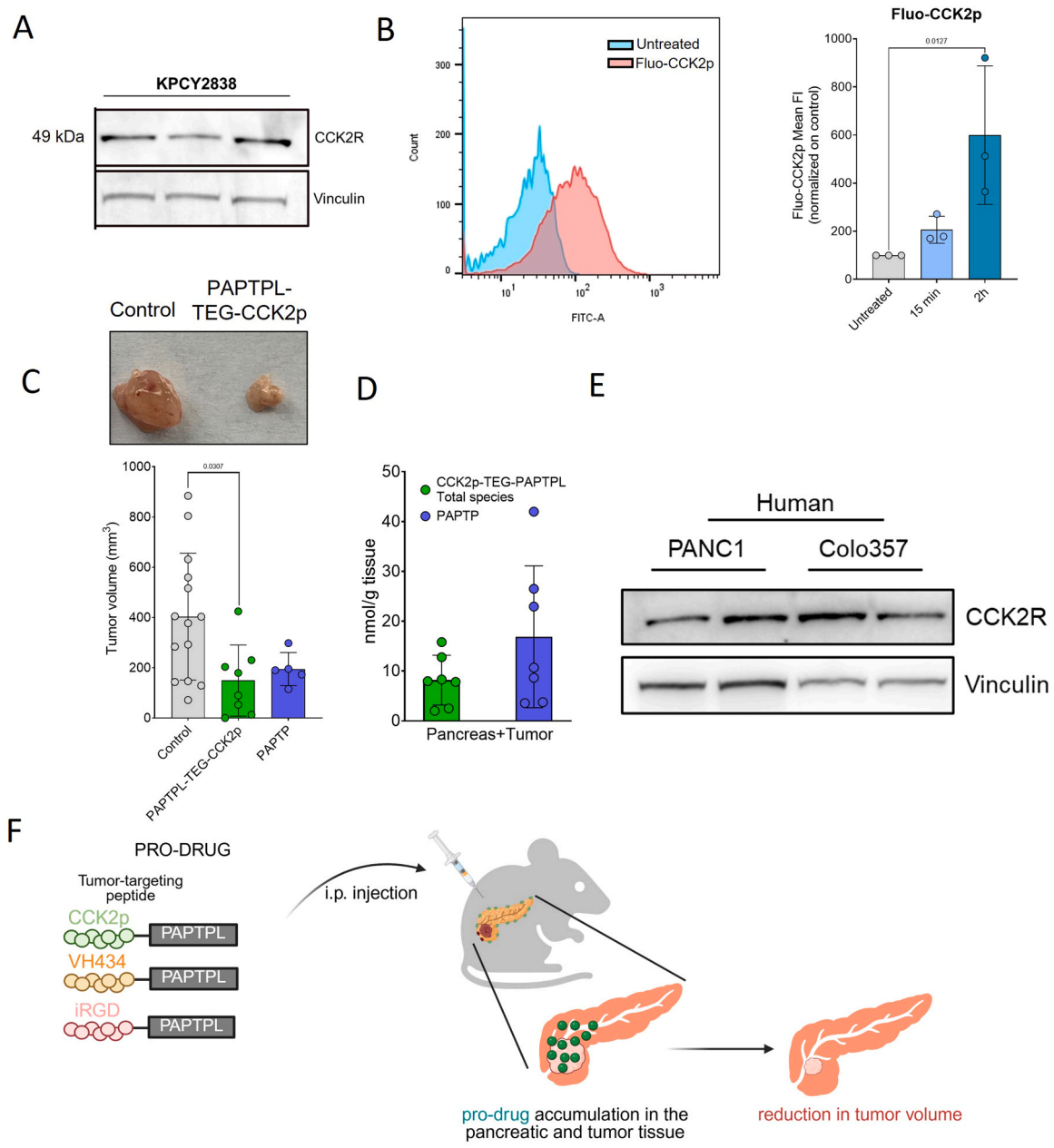


Fig. 6. Tumor volume reduction by PAPTPL-TEG-CCK2p in KPC orthotopic model. Expression of CCKR2 in three lysates of cultured KPCY2838c3 cells (Western blot using an antibody targeting the human form of CCK2R). B) Uptake of Fluo-CCK2p into non-fluorescent KPC cells, assessed by flow cytometry. Kruskal-Wallis; significance is shown C) Representative images of untreated and treated tumors, as indicated. Right: Tumor volume of KPCY2838c3 orthotopic PDAC model upon the indicated treatments. Kruskall-Wallis; significance is shown. D) Quantification of the total species of PAPTPL-TEG-CCK2p and of PAPTP at the endpoint of the experiment (animals were sacrificed 6 h after the last administration of the drugs). E) Western blot analyses of CCK2R protein levels (with an antibody targeting the human form of CCK2R) in lysates of cultured PANC1 and Colo357 cells. F) Summarizing figure of the findings. Among the three tumor-targeting peptide-PAPTPL constructs the CCk2p-PAPTPL construct proved to be suitable for in vivo experiments. The tumor size was significantly decreased by PAPTPL which was targeted specifically to the tumor thanks to the CCK2p peptide.

PaCa-2, and PANC-1 PDAC cells significantly reduced proliferation [88]. Most importantly, examining a cohort of 51 PDAC patients, Smith and colleagues identified a single nucleotide polymorphism of CCK2R (CCKBR) receptor and of its alternatively spliced isoform (CCKCR) that predicts the risk for pancreatic cancer [89]. Collectively, these studies suggest that CCK2R is expressed at a significant level in human PDAC cells and our data showing expression of CCK2R in PANC-1 and Colo-357 human PDAC lines confirm these results. However, the TCGA database indicates that the expression of this receptor is low in patients with PAAD and CCK2R was found to be expressed in other studies only in a subset of patients harbouring pancreatic cancer of neuroendocrine origin [54] while another study reported high expression of CCK2R in both normal and tumoral pancreatic tissues [90].

In summary, the construct developed by us might be useful for human PDACs provided the cells express CCK2R. Independently of PDAC, the translational potential of the pro-drug described here is enhanced by the observation that CCK2R overexpression has been detected in a variety of tumors, including medullary thyroid cancer (>90 % cases), stromal ovarian cancer (100 % incidence), and small cell lung cancer (56 % incidence) [91]. Therefore, future studies might be warranted to test expression level of Kv1.3 in these tumor types and test our construct in primary and metastatic tumors. In addition, the strategy

described here may be useful also for other mitochondria-targeted channel inhibitors, for example mito-TRAM34, acting on mitochondrial KCa3.1 and able to reduce PDAC in orthotopic models [92]. This option is particularly interesting, as KCa3.1 has a sixfold higher expression in pancreatic cancer tissues compared to healthy tissues according to the TCGA dataset (not shown).

In conclusion, evidence was provided that a small molecule inhibitor of a mitochondrial potassium channel can be efficiently targeted to PDAC via tumor-targeting peptides. Nevertheless, a limitation to the generalizability of the study is that it did not consider gender/sex issues. The findings of this study highlight the potential for toxicity arising from the hemolytic activity of peptide-small molecule conjugates. Furthermore, it is noteworthy that unexpected cleavage of the targeting molecules may occur, contingent on the cargo. It is evident that the field of peptide-conjugated drugs and proteins, which have been demonstrated to modulate the activities of cancer cells and immune cells within the TME (see e.g. [93]) is undergoing rapid development and shows great promise. Consequently, there is a high probability of the development of additional tumor-targeting peptides that are compatible with conjugation to small drugs, resulting in enhanced efficiency, in the near future.

4. Materials and methods

4.1. Gene expression profiling interactive analysis (GEPIA)

GEPIA (gene expression profiling interactive analysis) (http://gepia.cancerpku.cn/, accessed on 13 August 2025) is an interactive web application for analysis of gene expression based on 9736 tumors and 8587 normal samples from TCGA and GTEx data [94]. GEPIA was used to analyse the expression of the genes mentioned in the results section in pancreatic adenocarcinoma (PAAD) and to determine their effects on overall survival by means of the Kaplan–Meier analysis.

4.2. Chemistry

4.2.1. Materials and Instruments

Fmoc-protected amino acids, preloaded 2-Cl-Trityl resin, and coupling reagents (HBTU and HOBt) were purchased from Iris Biotech (Marktredwitz, Germany). Other reagents and solvents were purchased from Sigma Aldrich (Milan, Italy), and were used as received.

Flash chromatography was performed on silica gel (Macherey-Nagel 60, 230–400 mesh granulometry (0.063–0.040 mm), Fisher Scientific Italia, Segrate (MI), Italy) under air pressure.

Preparative HPLC was performed using a Shimadzu LC-8 system (Shimazdu, Kyoto, Japan) with a C18 column (Vydac 218TP1022, 10 μm, 250 × 22 mm). The column was perfused at a flow rate of 12 mL/min with a mobile phase consisting of eluent A (0.05 % TFA in water) and B (0.05 % TFA in 9:1 v/v acetonitrile:water); eluent B was increased over time following a linear gradient. Preparative HPLC was also performed using an Agilent 1290 Prep LC instrument, equipped with a double pump LC8A and a UV-Visible detector (SPD20A Prominence, set at 254 nm) using a semi-preparative column (Agilent Zorbax Eclipse PrepHT XDB-C18, 5 μm, 250 × 21.2 mm), solvents A and B were respectively H_2O + 0.1 % TFA and ACN. The method used was from 5 % B to 100 % B in 30 min.

Analytical HPLC analyses were performed on a Shimadzu LC-10 instrument fitted with a Jupiter C18 column (10 μm, 250 × 4.6 mm Phenomenex, Torrance, CA, USA) using the above eluent system (eluents A and B), flow rate of 1 mL/min, detection at 216 nm. UPLC analyses were conducted with an Agilent 1290 Infinity system equipped with a DAD detector (λ = 190–400 nm) and a ZORBAX Eclipse XDB-C18 (2.1 × 50 mm, 1.8 μm) column. The mobile phase used was: phase A water + 0.1 % TFA, mobile phase B ACN + 0.1 % TFA, gradient starting from 5 % B and reaching 100 % B in 10 min, flow rate of 0.6 mL/min. Detection at 254 nm.

^1H and ^{13}C nuclear magnetic resonance (NMR) spectra were recorded with a Bruker 500 Avance III operating at 500 MHz (for ^1H NMR) and 126 MHz (for ^{13}C NMR) or with a Bruker Avance III HD 400 spectrometer operating at 400 MHz (for ^1H NMR) and 101 MHz (for ^{13}C NMR). Chemical shifts (δ) are given in parts per million (ppm) relative to the signal of the solvent. The following abbreviations are used to indicate multiplicities: d, doublet; t, triplet; m, multiplet.

Electrospray ionization-mass spectrometry (ESI-MS) analysis was carried out with a Mariner mass spectrometer (PerSeptive Biosystem, Framingham, MA, USA) or a 1100 Series Agilent Technologies system (Agilent Technologies, Milan, Italy). The ESI source operated in full-scan positive ion mode, applying the following ESI parameters: nebulizer pressure 20 psi, dry gas flow 5 L/min, dry gas temperature 325 °C. The flow rate was 0.05 mL/min. High resolution electrospray ionization-mass spectrometry (HR-ESI-MS) was carried out using a Xevo G2-XS QTof in positive ioniziation mode.

Microwave-assisted syntheses were performed in a CEM Discover® monomode reactor (CEM Srl, Cologno Al Serio (BG), Italy) with the temperature monitored by a built-in infrared sensor.

4.2.2. Peptide synthesis

Peptides (iRGD, VH434 and CCK2) were synthesized manually using solid phase Fmoc chemistry on a 0.06 mmoles scale, employing appropriate resins. HATU or HBTU/HOBt was employed as activator, utilizing a three-fold molar excess (0.24 mmol) of Fmoc-amino acids in DMF (N, N-dimethylformamide) for each coupling cycle, unless otherwise indicated. The duration of the coupling process was 40 min. Fmoc deprotection was performed with 20 % piperidine in DMF. Coupling yields were monitored on aliquots of peptide-resin by evaluation of Fmoc displacement. At the conclusion of the peptide synthesis, prior to the detachment of the peptides from the resin, the 5-hexynoic acid is condensed to the N-terminal amino group of each peptide, in accordance with the procedures previously delineated.

The process of peptide cleavage from the resin is concurrent with the deprotection of the peptides by treatment with a mixture of TFA-triisopropylsilane-H_2O (96:3:1 v/v) for a duration of 45 min at ambient temperature.

The side-chain to side-chain cyclic peptides (iRGD and VH434) were obtained by means of oxidation of the Cys thiol groups with DMSO. In summary: 4 mL of DMSO are added to 80 mL of a 0.5 mM peptide solution in 10 mM ammonium acetate, pH 7.0. The reaction is then stirred at room temperature for a period of four hours. Following this, the solution is freeze-dried until the complete removal of the DMSO is achieved.

Peptides were purified by preparative reversed-phase HPLC. The fractions containing the desired products were collected and lyophilized to constant weight. All peptides showed less than 1 % impurities. The molecular weights of the compounds were determined by ESI-MS.

The sequence of the synthesized peptide derivatives (Hex = 5-hexynoic acid) were the followings:

Hex-$_c$(Cys-Met-Pro-Arg-Leu-Arg-Gly-Cys)-NH_2 VH434
Hex-βAla-βAla-$_c$(Cys-Arg-Gly-Asp-Arg-Gly-Pro-Asp-Cys)-OH iRGD
Hex-His-Glu-Ala-Tyr-Gly-Trp-Met-Asp-Phe-NH_2 CCK2

4.2.3. PAPTPL-Teg-N_3 Synthesis

PAPTPL-Teg-N_3 Synthesis was performed as described in Parrasia et al. [32].

Synthesis of 4-nitrophenyl (14-azido-3,6,9,12-tetraoxatetradecyl)carbamate (1)

The compounds 14-azido-3,6,9,12-tetraoxatetradecan-1-amine (500 mg, 1.91 mmol, 1 eq.), 4-dimethylaminopyridine (DMAP) (466 mg, 3.81 mmol, 2 eq.), and bis(4-nitrophenyl)carbonate (640 mg, 2.10 mmol, 1.1 eq.) were dissolved in CH_3CN (7.5 mL). The mixture was stirred for 3 h at 50 °C, then the solvent was removed under reduced

pressure. The concentrated mixture was dissolved in DCM (50 mL) and washed with 0.5 M HCl (50 mL). The aqueous phase was extracted with DCM (3×50 mL) and the total organic phase was dried over sodium sulfate. The solvent was removed under reduced pressure and the crude product was purified by flash chromatography (DCM:acetone, 9:1 as eluent) to afford **1** (484 mg, 1.13 mmol, 59 % yield) as a transparent oil (Scheme 1 and 2). ^{1}H NMR (500 MHz, CDCl3) δ 8.25–8.18 (m, 2 H), 7.33–7.27 (m, 2 H), 6.12–6.00 (m, 1 H), 3.69–3.60 (m, 16 H), 3.48–3.43 (m, 2 H), 3.38–3.33 (m, 2 H). ^{13}C NMR (126 MHz, $CDCl_3$) δ 156.17, 153.39, 144.76, 125.16, 122.09, 70.76, 70.71, 70.64, 70.62, 70.38, 70.09, 69.71, 50.71, 41.25. ESI-MS (m/z): 428.1 (calculated 428.2) $[M + H]^+$, 445.2 (calculated 445.2) $[M + NH_4]^+$, 450.1 (calculated 450.2) $[M + Na]^+$.

Synthesis of (4-(3-(4-(((14-azido-3,6,9,12-tetraoxatetradecyl)carbamoyl)oxy)phenyl)propoxy)phenyl)(3-(4-(4-((7-oxo-7H-furo [3,2-g]chromen-4-yl)oxy)butoxy)phenyl)propyl)diphenylphosphonium 2,2,2-trifluoroacetate (PAPTPL-TEG-N$_3$)

PAPTPL was synthesized as described in Parrasia et al. [58]. PAPTPL (321 mg, 350 μmol, 1 eq.), intermediate **1** (299 mg, 700 μmol, 2 eq.) and DMAP (85.5 mg, 700 μmol, 2 eq.) were dissolved in CH_3CN (3.0 mL). The mixture was stirred for 95 h at 50 °C, then the solvent was removed under reduced pressure. The concentrated mixture was dissolved in DCM (50 mL) and washed with 0.5 M HCl (50 mL). The aqueous phase was extracted with DCM (2 × 50 mL) and the total organic phase was dried over sodium sulfate. The solvent was removed under reduced pressure and the crude product was purified by flash chromatography (eluents: DCM:acetone, 9:1 v/v to remove impurities, then DCM:MeOH, 8:2 v/v to get the desired product) to yield PAPTPL-Teg-N_3 (392 mg, 326 μmol, 93 % yield) as a slightly yellow viscous oil. ^{1} H NMR (500 MHz, $CDCl_3$) δ 8.12 (d, J = 9.8 Hz, 1 H), 7.76 (t, J = 7.2 Hz, 2 H), 7.67–7.54 (m, 9 H), 7.53–7.46 (m, 2 H), 7.15 (d, J = 8.3 Hz, 2 H), 7.12–7.06 (m, 3 H), 7.06–6.99 (m, 4 H), 6.95 (d, J = 1.6 Hz, 1 H), 6.79 (d, J = 8.3 Hz, 2 H), 6.18 (d, J = 9.8 Hz, 1 H), 5.88 (t, J = 5.4 Hz, 1 H), 4.52 (t, J = 5.9 Hz, 2 H), 4.07–3.98 (m, 4 H), 3.70–3.57 (m, 16 H), 3.47–3.39 (m, 2 H), 3.35 (t, J = 4.9 Hz, 2 H), 3.27–3.16 (m, 2 H), 2.82–2.72 (m, 4 H), 2.15–1.95 (m, 6 H), 1.94–1.82 (m, 2 H). ^{13} C NMR (126 MHz, CDCl3) δ 164.49 (d, J_{C-P} = 3.0 Hz), 161.34, 158.36, 157.63, 155.05, 152.73, 149.53, 149.04, 145.00, 139.50, 137.88, 135.53 (d, J_{C-P} = 11.5 Hz), 135.10 (d, J_{C-P} = 2.8 Hz), 133.32 (d, J_{C-P} = 9.9 Hz), 131.86, 130.51 (d, J_{C-P} = 12.5 Hz), 129.84, 129.29, 121.74, 118.80 (d, J_{C-P} = 86.6 Hz), 116.84 (d, J_{C-P} = 13.7 Hz), 114.72, 113.30, 112.47, 106.99 (d, J_{C-P} = 93.7 Hz), 106.72, 105.27, 93.82, 72.63, 70.75, 70.71, 70.67, 70.64, 70.62, 70.37, 70.06, 69.93, 67.68, 67.42, 50.73, 41.12, 34.99 (d, J_{C-P} = 16.6 Hz), 31.37, 30.42, 27.00, 26.00, 24.56 (d, J_{C-P} = 3.7 Hz), 21.67 (d, J_{C-P} = 52.7 Hz). ESI-MS (m/z): 1091.6 (calculated 1091.5) $[M]^+$, 557.2 (calculated 557.2) $[M + Na]^{2+}$, 565.2 (calculated 565.2) $[M + K]^{2+}$ (Table 1).

4.2.4. Synthesis of PAPTPL-TEG-iRGD, PAPTPL-TEG-VH434, PAPTPL-TEG-CCK2

PAPTPL-TEG-N_3 (23.6 mg, 19.6 μmol, 1 eq.) and peptide-alkyne (19.6 μmol, 1 eq.) were dissolved in tert-butanol:H_2O:THF 1:1:1 v/v (450 μL) (Scheme 2). A mixture of 1.0 M sodium ascorbate in water (19.6 μL, 19.6 μmol, 1 eq.) and 1.0 M $CuSO_4$ in water (19.6 μL, 19.6 μmol, 1 eq.) was added. The mixture was stirred for 20 h at room temperature in a sealed vial under nitrogen atmosphere. The crude product was purified by preparative HPLC to yield the desired PAPTPL-TEG-peptide as a white powder.

4.2.5. Synthesis of NBDTP-TEG-CCK2p fluorescent derivative (Fluo-CCK2p)

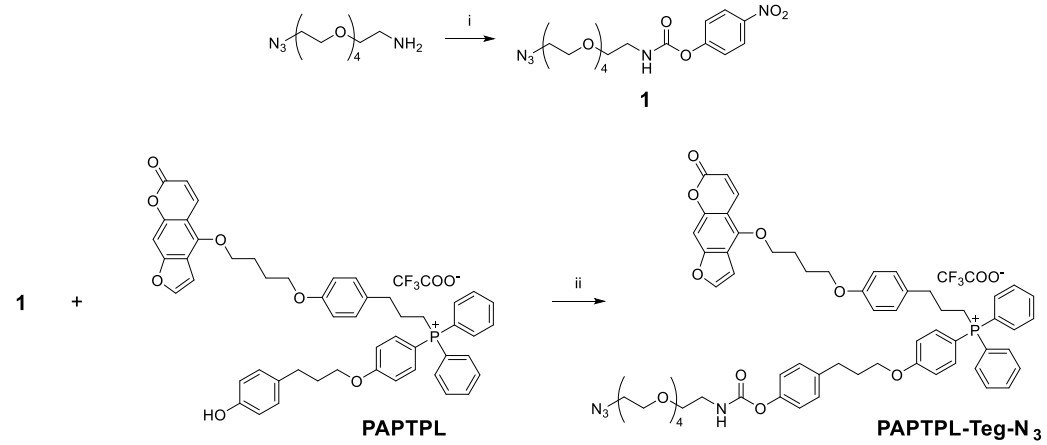
NBDTP-TEG-CCK2p was synthesized via a convergent strategy. The fluorophore-containing intermediate **5** and the triphenylphosphine-functionalized oligoethylene glycol spacer **7** were prepared independently, as shown in Scheme 3 (panels A and B, respectively). These intermediates were then combined to afford the phosphonium intermediate **8**, which was subjected to tosylation followed by substitution with sodium azide (NaN_3), enabling subsequent copper-catalyzed azide–alkyne cycloaddition (CuAAC) with the CCK2 hexynyl peptide (Scheme 3C).

Synthesis of 3-(4-(4-chlorobutoxy)phenyl)propan-1-ol (1)

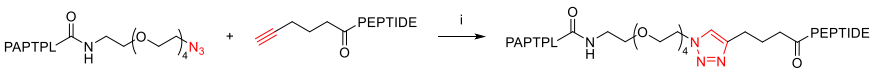
A solution of 4-(3-hydroxypropyl)phenol (1.0 g, 6.57 mmol, 1.0 eq.) in DMF (4.24 mL) was treated with 1-chloro-4-iodobutane (1.74 mL, 15.11 mmol, 2.3 eq.) and K_2CO_3 (2.3 g, 16.43 mmol, 2.5 eq.). The reaction mixture was stirred at room temperature for 16 h, diluted with DCM (20 mL), and washed with brine (3 × 25 mL). The organic layer was dried over Na_2SO_4, filtered, and concentrated under reduced pressure. The residue was purified by silica gel flash chromatography (PE/EtOAc, 8:2) to afford **1** as a colorless oil (1.25 g, 5.13 mmol, yield: 78 %). **^{1}H NMR** (400 MHz, $CDCl_3$) δ 7.13 (d, *J* = 8.6 Hz, 2 H), 6.84 (d, *J* = 8.6 Hz, 2 H), 3.99 (t, *J* = 5.7 Hz, 2 H), 3.65 (m, 4 H), 2.66 (dd, *J* = 8.6, 6.8 Hz, 2 H), 2.05–1.83 (m, 7 H). **^{13}C NMR** (101 MHz, $CDCl_3$) δ 157.10, 134.00, 129.33, 114.43, 67.01, 62.20, 44.82, 34.43, 31.16, 29.37, 26.73. **ESI-MS** (m/z): 153.0 (calculated 153.1) $[M + H]^+$.

Synthesis of 3-(4-(4-azidobutoxy)phenyl)propan-1-ol (2)

1 (5.6 g, 22.9 mmol, 1.0 eq.) was dissolved in DMF (40 mL), and NaN_3 (4.5 g, 68.7 mmol, 3.0 eq.) was added. The mixture was heated at 70 °C and stirred for 16 h. After partial evaporation of the solvent at reduced pressure (to decrease the DMF quantity), the mixture was



Scheme 1. Synthesis of PAPTPL-Teg-N_3. Reagents and conditions: i) bis(4-nitrophenyl) carbonate, DMAP, CH_3CN, 50 °C for 3 h, 59 % yield; ii) intermediate 1, DMAP, CH_3CN, 50 °C for 95 h, 93 % yield.



Scheme 2. Synthesis of the PAPTPL-TEG-peptide derivatives. Reagents and conditions: i) $CuSO_4.5H_2O$; Sodium L-Ascorbate; H_2O:tBuOH:THF, RT, 20 h.

Table 1
Calculated and measured molecular masses of the indicated derivatives.

Derivative	*Yield %*	*Base Peak*	*m/z*	
			Calculated	Found
PAPTPL-TEG-iRGD	56	$[M+H]^{2+}$	1152.5	1152.4
PAPTPL-TEG-VH434	21	$[M]^+$	2117.9	2118.1
PAPTPL-TEG-CCK2p	52	$[M]^+$	2339.9	2340.0

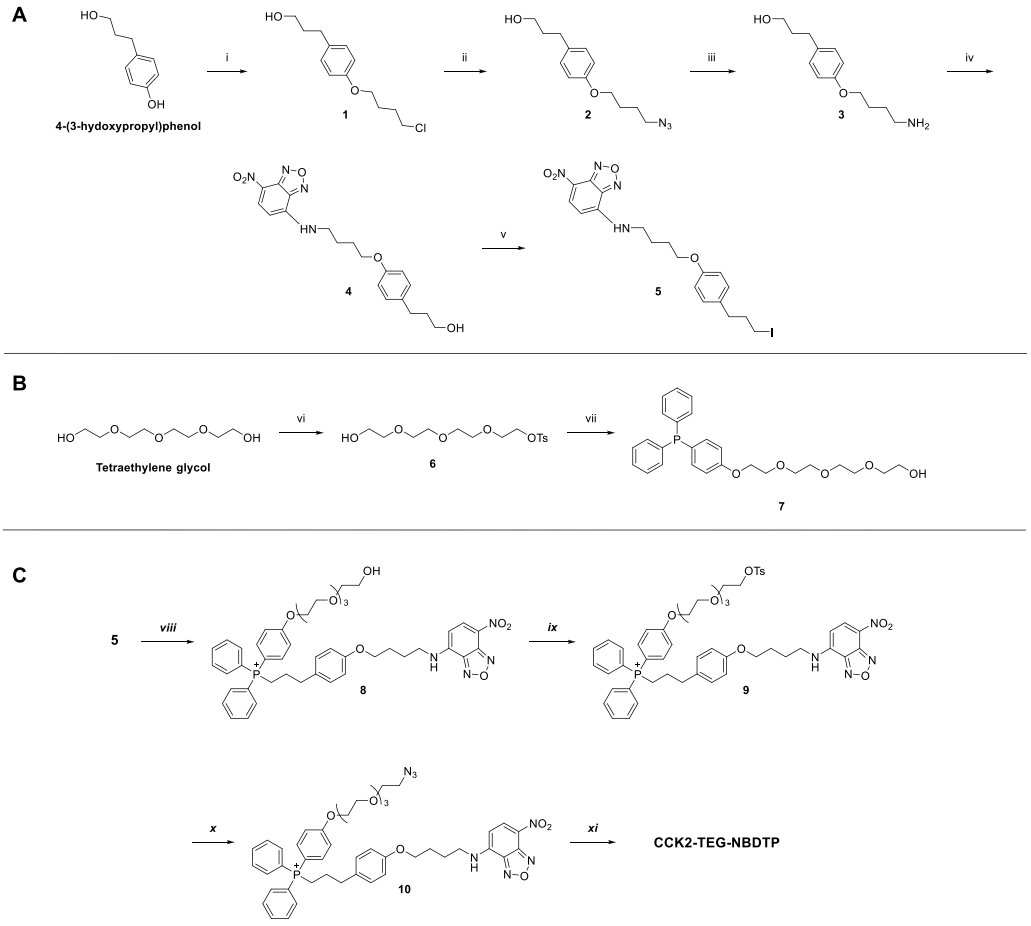
diluted with EtOAc (60 mL) and washed with brine (3 × 20 mL), then the organic layer was evaporated at reduced pressure and the residue was purified by silica gel flash chromatography (PE/EtOAc, 7:3) to yield **2** as a colorless oil (5.44 g, 22 mmol, yield: 96 %). **^{1}H NMR** (400 MHz, $CDCl_3$) δ 7.10 (d, J = 8.7 Hz, 2 H), 6.81 (d, J = 8.7 Hz, 2 H), 3.96 (t, *J* = 5.9 Hz, 2 H), 3.66 (t, *J* = 6.4 Hz, 2 H), 3.36 (t, *J* = 6.6 Hz, 2 H), 2.64 (dd, *J* = 8.6, 6.8 Hz, 2 H), 1.91 – 1.73 (m, 6 H). **^{13}C NMR** (101 MHz, $CDCl_3$) δ 157.08, 133.98, 129.33, 114.43, 67.18, 62.25, 51.22, 34.42, 31.15, 26.54, 25.78. **ESI-MS** (m/z): 243.0 (calculated 243.1) $[M + H]^+$.

Synthesis of 3-(4-(4-aminobutoxy)phenyl)propan-1-ol (3)

A solution of **2** (5.5 g, 22.0 mmol, 1.0 eq.) in THF (50 mL) was stirred at 0 °C under N_2. Separately, $LiAlH_4$ (2.5 g, 65.4 mmol, 3.0 eq.) was suspended in THF (100 mL) and added dropwise. After 15 min, TLC confirmed complete consumption of the starting material. Excess $LiAlH_4$ was quenched by dropwise addition of H_2O (1.2 mL), 8 M NaOH (1.2 mL), and H_2O (1.3 mL). The mixture was diluted with Et_2O (100 mL), dried over Na_2SO_4, filtered through celite, and evaporated at reduced pressure obtaining **3** as a colorless oil (4.2 g, 20.4 mmol, yield: 93 %). **^{1}H NMR** (400 MHz, $CDCl_3$) δ 7.10 (d, *J* = 8.5 Hz, 2 H), 6.82 (d, *J* = 8.6 Hz, 2 H), 3.95 (t, *J* = 6.4 Hz, 2 H), 3.67 (t, *J* = 6.4 Hz, 2 H), 2.77 (t, *J* = 7.0 Hz, 2 H), 2.65– 2.62 (m, 2 H), 1.91 – 1.77 (m, 4 H), 1.66 – 1.57 (m, 2 H). **^{13}C NMR** (101 MHz, $CDCl_3$) δ 157.92, 129.96, 115.12, 68.44, 62.96, 42.65, 35.13, 31.84, 31.07, 31.00, 27.41, 27.39. **ESI-MS** (m/z): 250.2 (calculated 250.2) $[M + H]^+$.

Synthesis of 3-(4-(4-((7-nitrobenzo[c][1,2,5]oxadiazol-4-yl)amino) butoxy)phenyl)propan-1-ol (4)

NBD-Cl (2.7 g, 13.4 mmol, 1.1 eq.) was dissolved in MeOH (67 mL) at 0 °C, followed by DIPEA (8.53 mL, 37.4 mmol, 4.0 eq.) and **3** (3.2 g, 14.3 mmol, 1.2 eq.). The mixture was stirred at r.t. for 5 h, diluted with EtOAc (80 mL), and washed with saturated NH_4Cl solution (3 × 40 mL).



Scheme 3. (A) Synthesis of N-(4-(4-(3-iodopropyl)phenoxy)butyl)-7-nitrobenzo[*c*] [1,2,5] oxadiazol-4-amine (**5**). Reagents and conditions: (i) 1-chloro-4-iodobutane, K_2CO_3, in DMF, 16 h, r.t.; (ii) NaN_3, in DMF, 16 h, 70 °C; (iii) $LiAlH_4$, in THF, 15 min, 0 °C; (iv) NBD-Cl, DIPEA, in MeOH, 5 h, r.t.; (v) imidazole, PPh_3, I_2, 16 h, r.t. (B) Synthesis of 2-(2-(2-(2-(4-(diphenylphosphaneyl)phenoxy)ethoxy)ethoxy)ethoxy)ethan-1-ol (**7**). Reagents and conditions: (vi) TsCl, DMAP, Py, in DCM, 18 h, r.t.; (vii) PPh_3-OH, Cs_2CO_3, in DMF, 2d, 50 °C. (C) Synthesis of NBDTP-TEG-CCK2p. Reagents and conditions: (viii) **7**, in toluene, 3 h, 80 °C; (ix) TsCl, DMAP, Py, in DCM, 16 h, r.t.; (x) NaN_3, in DMF, 16 h, 80 °C; (xi) Hexynyl-CCK2, CuI, Ascorbic Acid, DIPEA, in DMSO, 16 h, r.t.

The organic layer was dried over Na_2SO_4 and evaporated at reduced pressure. The residue was purified by silica gel flash chromatography (DCM/MeOH, 97:3) to afford **4** as an orange oil (4.0 g, 10.4 mmol, yield: 78 %). **^{1}H NMR** (400 MHz, $CDCl_3$) δ 8.47 (d, J = 8.6, 1 H), 7.11 (d, J = 8.6 Hz, 2 H), 6.83 (d, J = 8.6 Hz, 2 H), 6.18 (d, J = 8.6 Hz, 1 H), 4.04 (t, J = 5.6 Hz, 2 H), 3.67 (t, J = 6.4 Hz, 2 H), 3.60 (q, J = 6.5 Hz, 2 H), 2.69 – 2.62 (m, 2 H), 2.09 – 1.91 (m, 4 H), 1.91 – 1.81 (m, 2 H). **^{13}C NMR** (101 MHz, $CDCl_3$) δ 157.48, 144.66, 144.61, 137.25, 135.10, 130.14, 115.13, 99.31, 67.91, 62.97, 44.43, 35.10, 31.86, 27.26, 26.19. **ESI-MS** (m/z): 387.4 (calculated 387.2) $[M + H]^+$.

Synthesis of N-(4-(4-(3-iodopropyl)phenoxy)butyl)-7-nitrobenzo[c][1,2,5]*oxadiazol-4-amine* (5)

4 (4.0 g, 10.41 mmol, 1.0 eq.) was dissolved in DCM (20 mL) at 0 °C. Imidazole (3.2 g, 12.5 mmol, 1.2 eq.), PPh_3 (3.6 g, 13.85 mmol, 1.3 eq.), and I_2 (3.2 g, 12.5 mmol, 1.2 eq.) were added sequentially. The reaction was warmed to room temperature and stirred for 16 h. After dilution with DCM (70 mL), the mixture was washed with brine (3 × 40 mL), dried over Na_2SO_4, and evaporated at reduced pressure. Purification by silica gel flash chromatography (PE/EtOAc, 7:3) afforded **5** as an orange oil (4.0 g, 8.12 mmol, yield: 78 %). **^{1}H NMR** (400 MHz, Acetone-d_6) δ 8.47 (d, *J* = 8.6, 1 H), 7.11 (d, *J* = 8.6 Hz, 2 H), 6.83 (d, *J* = 8.6 Hz, 2 H), 6.18 (d, *J* = 8.6 Hz, 1 H), 4.04 (t, *J* = 5.6 Hz, 2 H), 3.67 (t, *J* = 6.4 Hz, 2 H), 3.60 (q, *J* = 6.5 Hz, 2 H), 2.69 – 2.62 (m, 2 H), 2.11 – 1.92 (m, 10 H). **^{13}C NMR** (101 MHz, Acetone-d_6) δ 156.89, 131.90, 128.74, 113.80, 66.51, 34.73, 34.37, 25.91, 5.48. **ESI-MS** (m/z): 497.0 (calculated 497.1) $[M + H]^+$.

Synthesis of 2-(2-(2-(2-hydroxyethoxy)ethoxy)ethoxy)ethyl 4-methylbenzenesulfonate (6)

To a solution of tetraethylene glycol (10.0 g, 52 mmol, 8.0 eq.) in DCM (33 mL) held at 0 °C, DMAP (1.6 g, 13 mmol, 2.0 eq.) and pyridine (1 mL, 13 mmol, 2.0 eq.) were added, followed after 10 min by TsCl (1.2 g, 6.4 mmol, 1.0 eq.) dissolved in DCM (10 mL). The mixture was stirred at room temperature for 18 h then was quenched by the addition at 0 °C of 2 M HCl (15 mL). The mixture was extracted with DCM (4 x 40 mL) and the combined organic fractions were dried over Na_2SO_4 and evaporated under reduced pressure. The residue was purified by silica gel flash chromatography (DCM/MeOH, 98:2) to give **6** as a colorless oil (0.82 g, 2.3 mmol, yield: 37 %). **^{1}H NMR** (400 MHz, $CDCl_3$) δ 7.78 – 7.74 (d, J = 8.3 Hz, 2 H), 7.31 (d, J = 8.3 Hz, 2 H), 4.16 – 4.10 (m, 2 H), 3.69 – 3.63 (m, 4 H), 3.63 – 3.58 (m, 4 H), 3.57 – 3.54 (m, 6 H), 2.41 (s, 3 H). **^{13}C NMR** (101 MHz, $CDCl_3$) δ 145.44, 133.52, 130.43, 128.54, 73.08, 71.27, 71.20, 71.00, 70.86, 69.86, 69.25, 62.25, 62.24, 22.21. **ESI-MS** (m/z): 349.0 (calculated 349.1) $[M + H]^+$.

Synthesis of 2-(2-(2-(2-(4-(diphenylphosphaneyl)phenoxy)ethoxy)ethoxy)ethoxy)ethan-1-ol (7)

PPh_3-OH (100 mg, 0.36 mmol, 1.0 eq.) was dissolved in DMF (1.64 mL) and treated with **6** (132 mg, 0.38 mmol, 1.05 eq.) and Cs_2CO_3 (141 mg, 0.43 mmol, 1.2 eq.). The mixture was stirred at 50 °C for 2 days under N_2. The mixture was diluted with DCM (20 mL) and washed with brine (4 × 5 mL), the organic layer was dried over Na_2SO_4, concentrated under reduced pressure and the residue was purified by silica gel flash chromatography (PE/EtOAc, 1:1) to yield **7** as a colorless oil (107 mg, 0.23 mmol, yield: 64 %). **^{1}H NMR** (400 MHz, $CDCl_3$) δ 7.37 – 7.23 (m, 12 H), 6.92 (dd, J = 8.9, J = 0.8, 2 H), 4.17 – 4.11 (m, 2 H), 3.89 – 3.84 (m, 2 H), 3.76 – 3.66 (m, 10 H), 3.63 – 3.58 (m, 2 H). **^{13}C NMR** (101 MHz, $CDCl_3$) δ 160.17, 138.49, 138.39, 136.28, 136.07, 134.36, 134.12, 133.94, 133.82, 133.66, 133.63, 129.32, 129.25, 129.11, 129.07, 129.04, 129.01, 128.84, 128.51, 128.42, 115.53, 115.45, 73.18, 71.39, 71.25, 71.16, 70.90, 70.24, 67.91, 62.29. **ESI-MS** (m/z): 455.0 (calculated 455.2) $[M + H]^+$.

Synthesis of (4-(2-(2-(2-(2-hydroxyethoxy)ethoxy)ethoxy)ethoxy)phenyl)(3-(4-(4-((7-nitrobenzo[c] [1,2,5]oxadiazol-4-yl)amino)butoxy)phenyl)propyl)diphenylphosphonium (8)

7 (81 mg, 0.178 mmol, 1.0 eq.) was reacted with **5** (88 mg, 0.178 mmol, 1.0 eq.) at 80 °C for 3 h in toluene (700 µL). After that time, the mixture was evaporated at reduced pressure and the residue was purified by silica gel flash chromatography (DCM/MeOH, 9:1) to yield **8** as a red solid (137 mg, 0.14 mmol, yield: 79 %). **^{1}H NMR** (400 MHz, MeOD) δ 8.35 (d, *J* = 8.9 Hz, 1 H), 7.87–7.56 (m, 13 H), 7.24 (dd, *J* = 9.0, 2.6 Hz, 2 H), 6.99 (d, *J* = 8.3 Hz, 2 H), 6.73 (d, *J* = 8.6 Hz, 2 H), 6.30 (d, *J* = 8.9 Hz, 1 H), 4.28 – 4.21 (m, 2 H), 3.99 (t, *J* = 5.7 Hz, 2 H), 3.88 – 3.83 (m, 2 H), 3.70 – 3.48 (m, 15 H), 2.78–2.70 (m, 2 H), 2.00 – 1.83 (m, 5 H). **^{13}C NMR** (101 MHz, MeOD) δ 165.62 (d, J_{C-P} = 3.0 Hz), 158.84, 136.91 (d, J_{C-P} = 12.0 Hz), 136.05, (d, J_{C-P} = 3.0 Hz), 134.65 (d, J_{C-P} = 10.0 Hz), 133.31, 131.45 (d, J_{C-P} = 12.0 Hz), 130.60, 120.48 (d, J_{C-P} = 87.0 Hz), 117.78 (d, J_{C-P} = 14.0 Hz), 115.67, 109.06 (d, J_{C-P} = 93.0 Hz), 99.92, 73.63, 71.69, 71.57, 71.52, 71.35, 70.38, 69.37, 68.36, 62.19, 44.56, 36.15 (d, J_{C-P} = 17.0 Hz), 27.78, 25.73 (d, J_{C-P} = 3.7 Hz), 22.54 (d, J_{C-P} = 52.5 Hz). **ESI-MS** (m/z): 823.5 (calculated 823.3) $[M]^+$.

Synthesis of (3-(4-(4-((7-nitrobenzo[c][1,2,5]*oxadiazol-4-yl)amino)butoxy)phenyl)propyl)diphenyl(4-(2-(2-(2-(2-(tosyloxy)ethoxy)ethoxy)ethoxy)ethoxy)phenyl)phosphonium* (9)

To a solution of **8** (127 mg, 0.134 mmol, 1.0 eq.) in DCM (2 mL) at 0 °C were added pyridine (32 µL, 0.397 mmol, 3.0 eq.), DMAP (33 mg, 0.268 mmol, 2.0 eq.), and TsCl (51 mg, 0.268 mmol, 2.0 eq.) and the mixture was stirred at room temperature for 16 h. After that time DCM (20 mL) was added and the mixture was washed with brine (3 × 10 mL). The organic layer was evaporated at reduced pressure and the residue purified by silica gel flash chromatography (DCM/MeOH, 98:2) to give **9** as a red solid (60 mg, 0.059 mmol, yield: 44 %). **^{1}H NMR** (400 MHz, MeOD) δ 8.34 (t, *J* = 8.2 Hz, 1 H), 7.87 – 7.78 (m, 2 H), 7.74 – 7.66 (m, 11 H), 7.60 (ddd, *J* = 12.1, 8.8, 6.0 Hz, 2 H), 7.36 (d, *J* = 8.0 Hz, 1 H), 7.27 – 7.15 (m, 4 H), 6.98 (dd, *J* = 8.6, 3.4 Hz, 2 H), 6.77 – 6.70 (m, 2 H), 6.26 (dd, *J* = 8.9, 5.8 Hz, 1 H), 4.28 – 4.19 (m, 2 H), 4.09 – 4.06 (m, 1 H), 3.98 (q, *J* = 5.7 Hz, 2 H), 3.85 (dtd, *J* = 7.1, 4.5, 2.9 Hz, 2 H), 3.73 –3.45 (m, 13 H), 3.31 – 3.21 (m, 2 H), 2.72 (td, *J* = 7.3, 3.4 Hz, 2 H), 1.99–1.82 (m, 6 H). **^{13}C NMR** (101 MHz, MeOD) δ 165.53, 165.50, 165.47, 158.73 (d, J_{C-P} = 1.2 Hz), 146.31, 143.61, 141.37, 136.72 (d, J_{C-P} = 11.4 Hz), 135.93 (d, J_{C-P} = 3.1 Hz), 134.47 (d, J_{C-P} = 10.0 Hz), 134.12, 133.16 (d, J_{C-P} = 0.8 Hz), 131.30 (d, J_{C-P} = 13.0 Hz), 130.93, 130.45 (d, J_{C-P} = 1.3 Hz), 129.65, 128.84, 126.84, 120.35, (d, J_{C-P} = 87.0 Hz), 117.73, 117.71, 117.59, 117.57, 115.54, 109.35 (d, J_{C-P} = 6.3 Hz), 108.42 (d, J_{C-P} = 6.0 Hz), 72.27, 71.60, 71.43, 71.40, 71.34, 71.32, 70.88, 70.26, 69.52, 69.24, (d, J_{C-P} = 1.7 Hz) 68.21, 43.82, 36.03 (d, J_{C-P} = 16.4 Hz), 27.64, 25.57, 25.55 (d, J_{C-P} = 3.9 Hz), 22.03, 21.52, 21.22. **ESI-MS** (m/z): 977.5 (calculated 977.4) $[M]^+$.

Synthesis of (4-(2-(2-(2-(2-azidoethoxy)ethoxy)ethoxy)ethoxy)phenyl)(3-(4-(4-((7-nitrobenzo[c][1,2,5]*oxadiazol-4-yl)amino)butoxy)phenyl)propyl)diphenylphosphonium* (10)

9 (68 mg, 0.067 mmol, 1.0 eq.) was dissolved in DMF (720 µL) and treated with NaN_3 (13 mg, 0.201 mmol, 3.0 eq.) and the mixture was heated at 80 °C for 16 h. After that time, it was diluted with DCM (40 mL), washed with water (10 mL), dried over Na_2SO_4, and evaporated at reduced pressure. Purification by silica gel flash chromatography (DCM/MeOH, 96:4) afforded **10** as a red solid (42 mg, 0.047 mmol, yield: 70 %). **^{1}H NMR** (400 MHz, MeOD) δ 8.41 (d, *J* = 8.8 Hz, 1 H), 7.86 (m, 2 H), 7.77 – 7.70 (m, 9 H), 7.70 – 7.59 (m, 2 H), 7.27 (dd, *J* = 9.0, 2.6 Hz, 2 H), 7.03 – 6.98 (m, 2 H), 6.77 (d, *J* = 8.6 Hz, 2 H), 6.32 (d, *J* = 8.9 Hz, 1 H), 4.32 – 4.25 (m, 2 H), 4.03 (t, *J* = 5.8 Hz, 2 H), 3.91 – 3.86 (m, 2 H), 3.33 (td, *J* = 4.0, 2.3 Hz, 4 H), 2.75 (t, *J* = 7.2 Hz, 2 H), 2.04 – 1.87 (m, 7 H). **^{13}C NMR** (101 MHz, MeOD) δ 166.32 (d, J_{C-P} = 3.1 Hz), 159.49, 137.46 (d, J_{C-P} = 11.4 Hz), 136.68 (d, J_{C-P} =

3.0 Hz), 135.21 (d, J_{C-P} = 10.0 Hz), 133.87 (d, J_{C-P} = 0.9 Hz), 132.03 (d, J_{C-P} = 12.5 Hz), 131.12, 121.56, 120.70, 118.37 (d, J_{C-P} = 13.8 Hz), 116.26, 110.13, 109.20, 72.36, 72.21, 72.09, 71.67, 71.01, 69.97, 68.89, 52.34, 40.73, 36.78 (d, J_{C-P} = 16.6 Hz) 28.38, 26.29 (d, J_{C-P} = 3.6 Hz), 23.35, 22.82. **ESI-MS** (m/z): 848.6 (calculated 848.4) $[M]^+$.

4.2.5.1. Synthesis of CCK2-TEG-NBDTP. **10** (6.5 mg, 0.0074 mmol, 1.0 eq.) was dissolved in DMSO (700 μL) and reacted with CCK2 hexynyl peptide (7.5 mg, 0.006 mmol, 0.81 eq.), CuI (1.4 mg, 0.0074 mmol, 1.0 eq.), ascorbic acid (2.6 mg, 0.015 mmol, 2.0 eq.), and DIPEA (10 μL, 7.64 mg, 0.059 mmol, 8.0 eq.). The mixture was stirred at room temperature for 16 h, filtered through PTFE, purified by preparative HPLC, and lyophilized to yield **CCK2-TEG-NBDTP** as an orange solid (5.6 mg, 0.0031 mmol, yield: 52 %). **HR-ESI-MS** (m/z)**:** 1048.8911 (calculated 1048.9353) $[M+H]^{2+}$. Purity by UPLC-UV-Vis > 95 %

4.3. Hemolysis assay

Erytrocytes were isolated from fresh mouse blood as described in [32]. Briefly, freshly withdrawn blood samples were centrifuged at 2000 × g for 10 min to obtain erythrocytes; the pellet was then washed three times with sterile PBS (pH 7.4). Erythrocytes (5×10^7 cells in 1 mL of PBS for each experimental condition) were incubated with the compounds at the concentrations of 1, 0.5, 0.25, or 0.125 nmoles/10^7 cells for 15 min. The samples were then centrifuged and the absorbance (Abs) of the supernatant was measured at 540 nm. Triton X-100 1 % and PBS were used as positive and negative control, respectively. The percentage of hemolysis was calculated with the following equation:

$$\% \text{ hemolysis} = [(Abs_{sample} - Abs_{PBS})/(Abs_{Triton\ X\text{-}100} - Abs_{PBS})] \times 100$$

4.4. Cell lines and crystal violet assay

All PDAC cell lines were cultured in DMEM (Gibco, 41966–029) supplemented with 10 % Fetal Bovine Serum (FBS) (Gibco, A5256701) supplemented with 1000 U/mL Penicillin and 1000 μg/mL Streptomycin (Gibco, 15140–122). Primary KPCY-derived cells were described in [63]. Pan02 and Colo357 were kindly donated by the PhIonic Marie Curie Training Network, KPCY2838c3, 266–6 and PANC1 were from the Carrer Laboratory.

For the evaluation of the IC_{50} of PAPTP and PAPTPL Pan02, KPCY2838c3 or 266–6 were seeded in a 96 well, respectively $3x10^4$ cell/well, $2x10^4$ cell/well and $3x10^4$ cell/well. The day after cells were treated with crescent concentrations (from 0,156 μM to 10 μM) of PAPTP or PAPTPL. After 24 h cells were fixed in 4 % PFA and stained with crystal violet. Crystal Violet (Merck #C0775; 0.1 % for 20 min) staining was performed according to manufacturer's instruction. After drying, crystal violet was solubilized with 10 % acetic acid and absorbance was measured using a Tecan infinite F200 PRO. IC_{50} was calculated using Prism Curve fitting.

4.5. Peptide uptake into pancreatic cancer cells

Pan02 and KPC (not expressing YFP) cells were seeded in 6-well plates at a density of 100,000 cells/well and grown for 48 h. They were then washed with PBS and left untreated or incubated for 15 min or 2 h at 37 °C with a solution of 5 μM Fluo-CCK2p in DMEM. At the end of the incubation, cells were washed, detached with trypsin, pelleted, and resuspended in 1 mL HBSS. After the treatment, mean fluorescence intensity was analyzed using BD Biosciences LRS Fortessa X20 flow cytometer (Franklin Lakes, NJ, USA). Subsequent data analysis was carried out using FlowJo Software (BD).

4.6. Mitochondrial membrane potential and mitochondrial ROS measurement

To measure mitochondrial membrane potential, KPCY2838 cells were incubated with 10 nM TMRM (ThermoFisher, T668) in HBSS (Gibco,14025) at 37 °C for 20 min. After incubation, basal TMRM fluorescence was visualized using Operetta and 5uM of the compounds (Fluo-CCK2p, PAPTPL) were added. For the PAPTPL-TEG-CCK2p, KPCY2838 cells were preincubated with 5uM of the compound overnight to allow the hydrolyzation. As control FCCP 1uM was added at the end of the experiment.

To measure mitochondria ROS production, Pan02 cells were preincubated with 5uM of the indicated compounds (Fluo-CCK2p, PAPTPL and Antimycin 2 h, PAPTPL-TEG-CCK2p overnight). Cells were then incubated with 5 μM of mitoSox (ThermoFisher, M36009) and 2 μM of CSH in HBSS (Gibco, 14025) at 37°C for 30 min. MitoSox fluorescence was measured by flow cytometry.

4.7. Mitochondrial morphology

To visualize mitochondrial morphology, KPCY2838 cells were seeded on ibidi chamber slides to allow live visualization using Leica Stellaris 8. Cells were incubated with 1 μM of MitoTracker Red (ThermoFisher, M7512) and Hoechest 3342 (ThermoFisher, H3570) at 37°C for 30 min. 5 μM of the compounds (Fluo-CCK2p, PAPTPL) were added and mitochondrial network was acquired every 5 min. For the PAPTPL-TEG-CCK2p, KPCY2838 cells were preincubated with 5 μM of the compound overnight to allow the hydrolysis by endogenous esterases.

4.7.1. Animals

C57Bl6/J mice were housed in the facility of the Department of Biology (Padova); food and water were provided ad libitum. All procedures were approved by the University of Padova Ethical Committee for Animal Welfare (OPBA) and by the Italian Ministry of Health (Permit Number 846/2021-PR), and conducted with the supervision of the Central Veterinary Service of the University of Padova, in compliance with Italian Law DL 26/2014, embodying EU Directive 2010/63/EU. All animal experiments comply with ARRIVE (Animal Research: Reporting of In Vivo Experiments) guidelines and the experiments complied with the EU recommendations (Directive 2010/63/EU) for experimental design and analysis in pharmacology care.

4.7.2. Orthotopic pancreatic cancer murine model

Eight-week-old, wild-type male, C57BL/6 J mice were purchased from Envigo RMS SRL. In detail, a left subcostal incision was made just below the rib cage and the pancreas was identified. 1×10^6 Pan02 cells with Matrigel (1:1) (Corning-CLS356234) were injected in the head of the pancreas. Pan02 cells were cultured in DMEM + 10 % FBS medium, under 37 °C and 5 % CO_2. The tumor suspension was slowly injected into the pancreas and the needle was left in place for 60 s to allow the Matrigel to set. After ensuring hemostasis, the abdomen was closed in 2 layers using 3–0 silk sutures. Wild-type mice were then randomly divided into 3 groups. Starting from 5 day after the orthotopic injection, mice were treated via IP every other day for 5 times with 5 nmol/g of vehicle (Kollifor), PAPTP or PAPTP-TEG-CCK2p. The day after the last injection, mice were sacrificed and tumors where harvested. Tumor volume, calculated as [hxl2]/2, was measured. For the tissue distribution of the PAPTPL-peptide constructs, 1×10^6 Pan02cells with Matrigel (1:1) (Corning-CLS356234) were injected in the head of the pancreas. 14 days after the orthotopic injection, mice were treated via IP with 4 nmol/g of fluorescent CCK2R-TEG-PAPTP and sacrificed 6 h later to evaluate the distribution of PAPTP in the tumor using the In Vivo Imaging System (IVIS®) Lumina S5™ (PerkinElmer) to detect the green fluorescence.

4.7.3. Liver metastatic model

Sub-confluent KPCY hot cells were trypsinized, washed, and resuspended in PBS. Cell suspensions (5x10^5 cells in 50 μl PBS) were injected into the spleen of 9-week-old wild-type C57BL/6 J mice, as reported by O'Brien and colleagues [60]. After 2 weeks post-injection, the mice were euthanized, and the tissues were lysed for Western blot analysis.

4.7.4. Western blotting

Cells were harvested and lysed in RIPA buffer (ThermoFisher scientific 89900), supplemented with protease inhibitor cocktail (Sigma-Aldrich P8340). Tumors and tissues were harvested and lysed in RIPA buffer (ThermoFisher scientific 89900), supplemented with protease inhibitor cocktail (Sigma-Aldrich P8340) using the TissueLyser II for 30 s at 1000 rpm. Protein concentration was measured using the Pierce™ BCA Protein Assay Kits (Thermo Fisher 23225). 25 μg of protein per sample were resolved on mPAGE® 4–12 % Bis-Tris Precast Gels (Merck MP41G12). After electrophoretic separation, proteins were transferred to and transferred to Immobilon®-P Membrane (Millipore IPVH85R). Membranes were incubated for 2–3 min at room temperature with a Pounceau Red 0.5 % (w/v) solution in 5 % (v/v) acetic acid (Merck Life Science S.r.l., Milan, Italy) for total protein staining. Images of the Pounceau Red staining were acquired in bright field using a Chemidoc Bio-rad apparatus. Membranes were then rinsed with milliQ water and destained with Tris-buffered saline buffer supplemented with 0.1 % Tween-20 (TBS-T; Merck Life Science S.r.l., Milan, Italy). The membranes were saturated for 20 min in TBST with 5 % nonfat milk (Merck Life Science S.r.l., Milan, Italy) and for 40 min in TBST with 5 % bovine serum albumin (Merck Life Science S.r.l., Milan, Italy), and then incubated overnight at 4°C with the primary antibody anti-CCK2R (Abcam ab183124, Abcam ab77077), anti-LDLR (Bioss, bs-0705R), anti-NRP1 (Santa Cruz Biotechnology, sc-5307), anti-Integrinβ5 (Abcam ab184312), anti-vinculin: Sigma-Aldrich, V4505). The following day, HRP-conjugated secondary (anti-mouse: Bio-Rad #1706516, anti-rabbit: Jackson ImmunoResearch 111–035–003) antibody were used at a dilution of 1:2000 for 1 h at RT. The chemiluminescence signal was detected using digital imaging by the Chemidoc Bio-rad apparatus (Bio-rad Laboratories, Milan, Italy).

4.7.5. Pharmacokinetics analysis

Pharmacokinetics analysis were performed in animals where PDAC was induced using Pan02 cells. 14 days after tumor induction, mice were administered with PAPTPL-TEG-CCK2p 5 nmol/gbw and sacrificed after 2, 6 or 14 h. After sacrifice, tumor, pancreas, spleen, liver, heart, kidney and blood were collected. Blood was immediately centrifuged for 10 min at 2000 g to obtain plasma. Organs were homogenized with PBS pH 7.4 (1 vol) with a potter and added with 5 vol of ACN containing 0.1 % trifluoracetic acid (TFA). The samples were sonicated for 5 min and then centrifuged at 12,000 × g for 7 min at 4°C. The supernatant was collected and analyzed via HPLC-UV.

4.7.6. Immunohistochemistry

Tissues were fixed in a 4 % PFA solution for 24 h, dehydrated with increasing alcohol solution and xylene and included in paraffin. After inclusion, 7 μm tumor sections were deparaffinized and rehydrated. Antigen retrieval was performed warming the sections into pre-warmed citrate buffer (10 mM, pH 6) in a microwave oven (160 W for 15 min). The sections were then stained using the Mouse To Mouse HRP kit (ScyTek Laboratories), according to the manufacturer's instructions. Ki67 was stained using anti-rabbit Ki67 primary antibody (Abcam ab16667). The sections were counterstained with hematoxylin and dehydrated. 8 fields were randomly captured from each section and analyzed Images analysis was performed with ImageJ software.

4.7.7. Hematoxylin and Eosin staining

7 μm tumor sections were deparaffinized, rehydrated and stained with Hematoxylin and Eosin according to the H&E staining kit (Rapid Frozen Section, BioOptica). Briefly, the sections were dipped in hematoxylin for 45 s, rinsed with tap water and dipped in the toning solution 5 times. Then, the sections were dipped in eosin for 30 s and dehydrated with ethanol 70 %, 90 %, 95 % and 100 % (2 min each) and with xylene for 5 min. Fields were randomly captured for each section with a Leica DM6 microscope (20x lens).

4.7.8. Tunel staining

Tumors derived from Pan02 orthotopic injection were formalin fixed for 24 h and then dehydrated and embedded in paraffin for histological evaluation. Then the embedded samples were sectioned at 4 μm. Tunel immunostaining (abcam ab206386) was performed following the manufacturer instructions and images were acquired using the DM6B Leica microscope.

CRediT authorship contribution statement

Alessandro Carrer: Writing – review & editing, Methodology, Funding acquisition. **Mostafa A.L Abdel-Salam:** Writing – review & editing, Validation, Investigation, Formal analysis, Data curation. **Erich Gulbins:** Writing – review & editing, Funding acquisition. **Valentina Brillo:** Writing – review & editing, Methodology. **Andrea Mattarei:** Writing – review & editing, Writing – original draft, Validation, Supervision, Methodology, Investigation, Formal analysis. **Mario Zoratti:** Writing – review & editing, Supervision, Formal analysis, Conceptualization. **Alberto Ongaro:** Writing – review & editing, Methodology, Formal analysis. **Lucia Biasutto:** Writing – review & editing, Writing – original draft, Validation, Supervision, Methodology, Formal analysis, Data curation, Conceptualization. **Paolo Ruzza:** Writing – review & editing, Validation, Supervision, Conceptualization. **Ildiko Szabo:** Writing – review & editing, Writing – original draft, Supervision, Project administration, Funding acquisition, Formal analysis, Conceptualization. **Beatrice Angi:** Writing – review & editing, Visualization, Investigation, Formal analysis. **Claudia Honisch:** Writing – review & editing, Supervision, Data curation. **Filippo Bergamin:** Methodology. **Magdalena Bachmann:** Writing – review & editing, Methodology, Investigation, Formal analysis, Data curation. **Elena Fiorini:** Methodology. **Sofia Parrasia:** Writing – review & editing, Visualization, Validation, Methodology, Investigation, Formal analysis, Data curation. **Vincenzo Corbo:** Writing – review & editing, Supervision, Resources. **Giovanna Bossio:** Investigation. **Tatiana Varanita:** Writing – review & editing, Visualization, Investigation, Data curation. **Andrea Rossa:** Methodology, Investigation, Data curation. **Carlotta Paoli:** Writing – review & editing, Visualization, Validation, Methodology, Investigation, Formal analysis, Data curation.

Declaration of Competing Interest

The authors declare no conflict of interest.

Acknowledgements

We are grateful to the Italian Association for Cancer Research (IG Grant IG 27271 to I.S.) for financial support and to the National Center for Gene Therapy and Drugs Based on RNA Technology, funded in the framework of the National Recovery and Resilience Plan (PNRR-CN 3), Mission 4, Component 2, Investment 1.4, funded by the European Union—Next Generation EU, Project CN00000041, CUP C93C22002780006, CN3, Spoke n.2, Cancer (I.S. and A.M.) as well as to ERC (Advanced Grant TRANSION to I.S.). I.S. E.G. and A.C. also thank World Wide Cancer Research WWCR (grant number 22–0348) for financial support. I.S. is also grateful to the Hu-rizont and pHIoniC International Training Network for support. M.B. and V.B. thank for AIRC fellowships (ID 25364 and ID 31563, respectively).

Appendix A. Supporting information

Supplementary data associated with this article can be found in the online version at doi:10.1016/j.phrs.2026.108150.

References

[1] R.L. Siegel, K.D. Miller, A. Jemal, Cancer statistics, 2020, CA Cancer J. Clin. 70 (1) (2020) 7–30.

[2] A. Bussetty, J. Shen, P.C. Benias, M. Ma, M. Stewart, A.J. Trindade, Incidence of pancreas and colorectal adenocarcinoma in the US, JAMA Netw. Open 8 (4) (2025) e254682.

[3] A.S. Bear, R.H. Vonderheide, M.H. O'Hara, Challenges and opportunities for pancreatic cancer immunotherapy, Cancer Cell 38 (6) (2020) 788–802.

[4] E. Fiorini, A. Malinova, D. Schreyer, D. Pasini, M. Bevere, G. Alessio, D. Rosa, S. D'Agosto, L. Azzolin, S. Milite, S. Andreani, F. Lupo, L. Veghini, S. Grimaldi, S. Pedron, M. Castellucci, C. Nourse, R. Salvia, G. Malleo, A. Ruzzenente, A. Guglielmi, M. Milella, R.T. Lawlor, C. Luchini, A. Agostini, C. Carbone, C. Pilarsky, A. Sottoriva, A. Scarpa, D.A. Tuveson, P. Bailey, V. Corbo, MYC ecDNA promotes intratumour heterogeneity and plasticity in PDAC, Nature 640 (8059) (2025) 811–820.

[5] P. Swietach, E. Boedtkjer, S.F. Pedersen, How protons pave the way to aggressive cancers, Nat. Rev. Cancer 23 (12) (2023) 825–841.

[6] M.H. Sherman, G.L. Beatty, Tumor microenvironment in pancreatic cancer pathogenesis and therapeutic resistance, Annu Rev. Pathol. 18 (2023) 123–148.

[7] Z. Hamel, S. Sanchez, D. Standing, S. Anant, Role of STAT3 in pancreatic cancer, Explor Target Antitumor Ther. 5 (5) (2024) 20–34.

[8] A. Scholz, S. Heinze, K.M. Detjen, M. Peters, M. Welzel, P. Hauff, M. Schirner, B. Wiedenmann, S. Rosewicz, Activated signal transducer and activator of transcription 3 (STAT3) supports the malignant phenotype of human pancreatic cancer, Gastroenterology 125 (3) (2003) 891–905.

[9] E. Prosdocimi, V. Carpanese, L.M. Todesca, T. Varanita, M. Bachmann, M. Festa, D. Bonesso, M. Perez-Verdaguer, A. Carrer, A. Velle, R. Peruzzo, S. Muccioli, D. Doni, L. Leanza, P. Costantini, F. Stein, M. Rettel, A. Felipe, M.J. Edwards, E. Gulbins, L. Cendron, C. Romualdi, V. Checchetto, I. Szabo, BioID-based intact cell interactome of the Kv1.3 potassium channel identifies a Kv1.3-STAT3-p53 cellular signaling pathway, Sci. Adv. 10 (36) (2024) eadn9361.

[10] L.A. Pardo, W. Stuhmer, The roles of K(+) channels in cancer, Nat. Rev. Cancer 14 (1) (2014) 39–48.

[11] M.D. Amico, L. Gasparoli, A. Arcangeli, Potassium channels: novel emerging biomarkers and targets for therapy in cancer, Recent Pat. Anticancer Drug Discov. 8 (1) (2013) 53–65.

[12] A. Teisseyre, A. Palko-Labuz, K. Sroda-Pomianek, K. Michalak, Voltage-Gated Potassium Channel Kv1.3 as a Target in Therapy of Cancer, 2019.

[13] N. Comes, J. Bielanska, A. Vallejo-Gracia, A. Serrano-Albarrás, L. Marruecos, D. Gómez, C. Soler, E. Condom, S. Ramón y Cajal, J. Hernández-Losa, J.C. Ferreres, A. Felipe, The voltage-dependent K+ channels Kv1.3 and Kv1.5 in human cancer, Front. Physiol. 4 (2013).

[14] E. Lastraioli, G. Perrone, A. Sette, A. Fiore, O. Crociani, S. Manoli, M. D'Amico, M. Masselli, J. Iorio, M. Callea, D. Borzomati, G. Nappo, F. Bartolozzi, D. Santini, L. Bencini, M. Farsi, L. Boni, F. Di Costanzo, A. Schwab, A. Onetti Muda, R. Coppola, A. Arcangeli, hERG1 channels drive tumour malignancy and may serve as prognostic factor in pancreatic ductal adenocarcinoma, Br. J. Cancer 112 (6) (2015) 1076–1087.

[15] V. Hofschröer, K. Najder, M. Rugi, R. Bouazzi, M. Cozzolino, A. Arcangeli, G. Panyi, A. Schwab, Ion channels orchestrate pancreatic ductal adenocarcinoma progression and therapy, Front Pharm. 11 (2020) 586599.

[16] B. Soret, J. Hense, S. Lüdtke, I. Thale, A. Schwab, M. Düfer, Pancreatic K(Ca)3.1 channels in health and disease, Biol. Chem. 404 (4) (2023) 339–353.

[17] A. Bararia, A. Maiti, G. Ghosh, D. Das, D.G. Dastidar, S. Mukherjee, S. Ghosh, B. K. Chattopadhay, S. Banerjee, S. Ghatak, N. Sikdar, Identification of KCNJ5 gene an adverse prognosis associated novel onco-ionchannel in Indian pancreatic cancer cohort, Discov. Oncol. 16 (1) (2025) 236.

[18] L. Leanza, M. Romio, K.A. Becker, M. Azzolini, L. Trentin, A. Managò, E. Venturini, A. Zaccagnino, A. Mattarei, L. Carraretto, A. Urbani, S. Kadow, L. Biasutto, V. Martini, F. Severin, R. Peruzzo, V. Trimarco, J.H. Egberts, C. Hauser, A. Visentin, G. Semenzato, H. Kalthoff, M. Zoratti, E. Gulbins, C. Paradisi, I. Szabo, Direct pharmacological targeting of a mitochondrial ion channel selectively kills tumor cells in vivo, Cancer Cell 31 (4) (2017) 516–531.e10.

[19] W. Li, G.C. Wilson, M. Bachmann, J. Wang, A. Mattarei, C. Paradisi, M.J. Edwards, I. Szabo, E. Gulbins, S.A. Ahmad, S.H. Patel, Inhibition of a mitochondrial potassium channel in combination with gemcitabine and abraxane drastically reduces pancreatic ductal adenocarcinoma in an immunocompetent orthotopic murine model, Cancers 14 (11) (2022).

[20] S.H. Patel, M. Bachmann, S. Kadow, G.C. Wilson, M.M.L. Abdel-Salam, K. Xu, S. Keitsch, M. Soddemann, B. Wilker, K.A. Becker, A. Carpinteiro, S.A. Ahmad, I. Szabo, E. Gulbins, Simultaneous targeting of mitochondrial Kv1.3 and lysosomal acid sphingomyelinase amplifies killing of pancreatic ductal adenocarcinoma cells in vitro and in vivo, J. Mol. Med. 101 (3) (2023) 295–310.

[21] S.H. Patel, G.C. Wilson, Y. Wu, S. Keitsch, B. Wilker, A. Mattarei, S.A. Ahmad, I. Szabo, E. Gulbins, Sphingosine is involved in PAPTP-induced death of pancreas cancer cells by interfering with mitochondrial functions, J. Mol. Med. 102 (7) (2024) 947–959.

[22] Y. Wang, Y. Zhang, J. Yang, X. Ni, S. Liu, Z. Li, S. E. Hodges, W. E. Fisher, F. C. Brunicardi, R. A. Gibbs, M.C. Gingras, M. Li, Genomic sequencing of key genes in mouse pancreatic cancer cells, Curr. Mol. Med. 12 (3) (2012) 331–341.

[23] A. Courtin, F.M. Richards, T.E. Bapiro, J.L. Bramhall, A. Neesse, N. Cook, B. F. Krippendorff, D.A. Tuveson, D.I. Jodrell, Anti-tumour efficacy of capecitabine in a genetically engineered mouse model of pancreatic cancer, PLoS One 8 (6) (2013) e67330.

[24] A. Zaccagnino, A. Manago, L. Leanza, A. Gontarewitz, B. Linder, M. Azzolini, L. Biasutto, M. Zoratti, R. Peruzzo, K. Legler, A. Trauzold, H. Kalthoff, I. Szabo, Tumor-reducing effect of the clinically used drug clofazimine in a SCID mouse model of pancreatic ductal adenocarcinoma, Oncotarget (2016).

[25] A. Schmitz, A. Sankaranarayanan, P. Azam, K. Schmidt-Lassen, D. Homerick, W. Hansel, H. Wulff, Design of PAP-1, a selective small molecule Kv1.3 blocker, for the suppression of effector memory T cells in autoimmune diseases, Mol. Pharmacol. 68 (5) (2005) 1254–1270.

[26] R. Peruzzo, A. Mattarei, M. Azzolini, K.A. Becker-Flegler, M. Romio, G. Rigoni, A. Carrer, L. Biasutto, S. Parrasia, S. Kadow, A. Managò, A. Urbani, A. Rossa, G. Semenzato, M.E. Soriano, L. Trentin, S. Ahmad, M. Edwards, E. Gulbins, C. Paradisi, M. Zoratti, L. Leanza, I. Szabò, Insight into the mechanism of cytotoxicity of membrane-permeant psoralenic Kv1.3 channel inhibitors by chemical dissection of a novel member of the family, Redox Biol. 37 (2020) 101705.

[27] V. Checchetto, L. Leanza, D. De Stefani, R. Rizzuto, E. Gulbins, I. Szabo, Mitochondrial K(+) channels and their implications for disease mechanisms, Pharm. Ther. 227 (2021) 107874.

[28] F. Severin, A. Urbani, T. Varanita, M. Bachmann, M. Azzolini, V. Martini, M. Pizzi, A.P.D. Tos, F. Frezzato, A. Mattarei, P. Ghia, M.T.S. Bertilaccio, E. Gulbins, C. Paradisi, M. Zoratti, G.C. Semenzato, L. Leanza, L. Trentin, I. Szabò, Pharmacological modulation of Kv1.3 potassium channel selectively triggers pathological B lymphocyte apoptosis in vivo in a genetic CLL model, J. Exp. Clin. Cancer Res. 41 (1) (2022) 64.

[29] S. Parrasia, M. Zoratti, I. Szabò, L. Biasutto, Targeting Pancreatic Ductal Adenocarcinoma (PDAC), Cell Physiol. Biochem. 55 (1) (2021) 61–90.

[30] I. Szabo, M. Zoratti, L. Biasutto, Targeting mitochondrial ion channels for cancer therapy, Redox Biol. 42 (2021) 101846.

[31] A. Rocchi, T. Teesalu, C. Celia, Advancing cancer-targeted nanotherapies with tumor homing peptides, ACS Pharm. Transl. Sci. 8 (7) (2025) 1919–1933.

[32] S. Parrasia, A. Rossa, N. Roncaglia, A. Mattarei, C. Honisch, I. Szabò, P. Ruzza, L. Biasutto, DA7R: a 7-letter zip code to target PDAC, Pharmaceutics 15 (5) (2023).

[33] T. Hurtado de Mendoza, E.S. Mose, G.P. Botta, G.B. Braun, V.R. Kotamraju, R. P. French, K. Suzuki, N. Miyamura, T. Teesalu, E. Ruoslahti, A.M. Lowy, K. N. Sugahara, Tumor-penetrating therapy for β5 integrin-rich pancreas cancer, Nat. Commun. 12 (1) (2021) 1541.

[34] T. Teesalu, K.N. Sugahara, V.R. Kotamraju, E. Ruoslahti, C-end rule peptides mediate neuropilin-1-dependent cell, vascular, and tissue penetration, Proc. Natl. Acad. Sci. USA 106 (38) (2009) 16157–16162.

[35] G. Balistreri, Y. Yamauchi, T. Teesalu, A widespread viral entry mechanism: the C-end Rule motif-neuropilin receptor interaction, Proc. Natl. Acad. Sci. USA 118 (49) (2021).

[36] A. Dean, S. Gill, M. McGregor, V. Broadbridge, H.A. Järveläinen, T. Price, Dual αV-integrin and neuropilin-1 targeting peptide CEND-1 plus nab-paclitaxel and gemcitabine for the treatment of metastatic pancreatic ductal adenocarcinoma: a first-in-human, open-label, multicentre, phase 1 study, Lancet Gastroenterol. Hepatol. 7 (10) (2022) 943–951.

[37] X. Liu, P. Lin, I. Perrett, J. Lin, Y.P. Liao, C.H. Chang, J. Jiang, N. Wu, T. Donahue, Z. Wainberg, A.E. Nel, H. Meng, Tumor-penetrating peptide enhances transcytosis of silicasome-based chemotherapy for pancreatic cancer, J. Clin. Invest. 127 (5) (2017) 2007–2018.

[38] V.M.D. Amore, G. Donati, E. Lenci, B.S. Ludwig, S. Kossatz, M. Baiula, A. Trabocchi, H. Kessler, F.S. Di Leva, L. Marinelli, Molecular view on the iRGD peptide binding mechanism: implications for integrin activity and selectivity profiles, J. Chem. Inf. Model 63 (20) (2023) 6302–6315.

[39] M. David, P. Lécorché, M. Masse, A. Faucon, K. Abouzid, N. Gaudin, K. Varini, F. Gassiot, G. Ferracci, G. Jacquot, P. Vlieghe, M. Khrestchatisky, Identification and characterization of highly versatile peptide-vectors that bind non-competitively to the low-density lipoprotein receptor for in vivo targeting and delivery of small molecules and protein cargos, PLoS One 13 (2) (2018) e0191052.

[40] Y. Molino, M. David, K. Varini, F. Jabès, N. Gaudin, A. Fortoul, K. Bakloul, M. Masse, A. Bernard, L. Drobecq, P. Lécorché, J. Temsamani, G. Jacquot, M. Khrestchatisky, Use of LDL receptor-targeting peptide vectors for in vitro and in vivo cargo transport across the blood-brain barrier, Faseb J. 31 (5) (2017) 1807–1827.

[41] X. Zhao, S. Long, M. Zhu, H. Hao, Y. Liao, C. Zhang, Z. Liu, Potential roles of SNX17, Rab11, and Rab5 in LDLR recycling, Arterioscler. Thromb. Vasc. Biol. 45 (8) (2025) e338–e354.

[42] A.J. Aguirre, N. Bardeesy, M. Sinha, L. Lopez, D.A. Tuveson, J. Horner, M. S. Redston, R.A. DePinho, Activated Kras and Ink4a/Arf deficiency cooperate to produce metastatic pancreatic ductal adenocarcinoma, Genes Dev. 17 (24) (2003) 3112–3126.

[43] F. Guillaumond, G. Bidaut, M. Ouaissi, S. Servais, V. Gouirand, O. Olivares, S. Lac, L. Borge, J. Roques, O. Gayet, M. Pinault, C. Guimaraes, J. Nigri, C. Loncle, M. N. Lavaut, S. Garcia, A. Tailleux, B. Staels, E. Calvo, R. Tomasini, J.L. Iovanna, S. Vasseur, Cholesterol uptake disruption, in association with chemotherapy, is a promising combined metabolic therapy for pancreatic adenocarcinoma, Proc. Natl. Acad. Sci. USA 112 (8) (2015) 2473–2478.

[44] A. Carrer, S. Trefely, S. Zhao, S.L. Campbell, R.J. Norgard, K.C. Schultz, S. Sidoli, J. L.D. Parris, H.C. Affronti, S. Sivanand, S. Egolf, Y. Sela, M. Trizzino, A. Gardini, B. A. Garcia, N.W. Snyder, B.Z. Stanger, K.E. Wellen, Acetyl-CoA metabolism supports multistep pancreatic tumorigenesis, Cancer Discov. 9 (3) (2019) 416–435.
[45] A. Acier, M. Godard, F. Gassiot, P. Finetti, M. Rubis, J. Nowak, F. Bertucci, J. L. Iovanna, R. Tomasini, P. Lécorché, G. Jacquot, M. Khrestchatisky, J. Temsamani, C. Malicet, S. Vasseur, F. Guillaumond, LDL receptor-peptide conjugate as in vivo tool for specific targeting of pancreatic ductal adenocarcinoma, Commun Biol. 4 (1) (2021) 987.
[46] M. Klingler, C. Decristoforo, C. Rangger, D. Summer, J. Foster, J.K. Sosabowski, E. von Guggenberg, Site-specific stabilization of minigastrin analogs against enzymatic degradation for enhanced cholecystokinin-2 receptor targeting, Theranostics 8 (11) (2018) 2896–2908.
[47] J.L. Abbruzzese, C.F. Gholson, K. Daugherty, E. Larson, R. DuBrow, R. Berlin, B. Levin, A pilot clinical trial of the cholecystokinin receptor antagonist MK-329 in patients with advanced pancreatic cancer, Pancreas 7 (2) (1992) 165–171.
[48] K.T. Cheng, (111)In-Tetraazacyclododecane-N,N',N'',N'''-tetraacetic acid-HHEAYGWMDF-NH(2) peptide, Molecular Imaging and Contrast Agent Database (MICAD), National Center for Biotechnology Information (US), Bethesda (MD), 2004.
[49] S. Good, M.A. Walter, B. Waser, X. Wang, J. Müller-Brand, M.P. Béhé, J.C. Reubi, H.R. Maecke, Macrocyclic chelator-coupled gastrin-based radiopharmaceuticals for targeting of gastrin receptor-expressing tumours, Eur. J. Nucl. Med. Mol. Imaging 35 (10) (2008) 1868–1877.
[50] J.P. Smith, L.K. Fonkoua, T.W. Moody, The role of gastrin and CCK receptors in pancreatic cancer and other malignancies, Int J. Biol. Sci. 12 (3) (2016) 283–291.
[51] J.P. Smith, T.K. Cooper, C.O. McGovern, E.L. Gilius, Q. Zhong, J. Liao, A. A. Molinolo, J.S. Gutkind, G.L. Matters, Cholecystokinin receptor antagonist halts progression of pancreatic cancer precursor lesions and fibrosis in mice, Pancreas 43 (7) (2014) 1050–1059.
[52] A. Mohammed, N.B. Janakiram, C. Suen, N. Stratton, S. Lightfoot, A. Singh, G. Pathuri, R. Ritchie, V. Madka, C.V. Rao, Targeting cholecystokinin-2 receptor for pancreatic cancer chemoprevention, Mol. Carcinog. 58 (10) (2019) 1908–1918.
[53] J.P. Smith, M.W. Hamory, M.F. Verderame, I.S. Zagon, Quantitative analysis of gastrin mRNA and peptide in normal and cancerous human pancreas, Int J. Mol. Med 2 (3) (1998) 309–315.
[54] J.C. Reubi, B. Waser, M. Gugger, H. Friess, J. Kleeff, H. Kayed, M.W. Büchler, J. A. Laissue, Distribution of CCK1 and CCK2 receptors in normal and diseased human pancreatic tissue, Gastroenterology 125 (1) (2003) 98–106.
[55] Y.P. Torres, F.J. Morera, I. Carvacho, R. Latorre, A marriage of convenience: beta-subunits and voltage-dependent K+ channels, J. Biol. Chem. 282 (34) (2007) 24485–24489.
[56] L. Solé, M. Roura-Ferrer, M. Pérez-Verdaguer, A. Oliveras, M. Calvo, J. M. Fernández-Fernández, A. Felipe, KCNE4 suppresses Kv1.3 currents by modulating trafficking, surface expression and channel gating, J. Cell Sci. 122 (20) (2009) 3738–3748.
[57] H. Sander, S. Wallace, R. Plouse, S. Tiwari, A.V. Gomes, Ponceau S waste: Ponceau S staining for total protein normalization, Anal. Biochem 575 (2019) 44–53.
[58] S. Parrasia, A. Rossa, T. Varanita, V. Checchetto, R. De Lorenzi, M. Zoratti, C. Paradisi, P. Ruzza, A. Mattarei, I. Szabò, L. Biasutto, An Angiopep2-PAPTP construct overcomes the blood-brain barrier. new perspectives against brain tumors, Pharmaceuticals 14 (2) (2021).
[59] F. Kruse, C.T. Komro, C.H. Michnoff, R.J. MacDonald, The cell-specific elastase I enhancer comprises two domains, Mol. Cell. Biol. 8 (2) (1988) 893–902.
[60] M. O'Brien, M. Ernst, A.R. Poh, An intrasplenic injection model of pancreatic cancer metastasis to the liver in mice, STAR Protoc. 4 (1) (2023) 102021.
[61] C. Jiang, H. Huang, X. Kang, L. Yang, Z. Xi, H. Sun, M.D. Pluth, L. Yi, NBD-based synthetic probes for sensing small molecules and proteins: design, sensing mechanisms and biological applications, Chem. Soc. Rev. 50 (13) (2021) 7436–7495.
[62] S. Suklabaidya, P. Dash, B. Das, V. Suresh, P.K. Sasmal, S. Senapati, Experimental models of pancreatic cancer desmoplasia, Lab Invest 98 (1) (2018) 27–40.
[63] J. Li, K.T. Byrne, F. Yan, T. Yamazoe, Z. Chen, T. Baslan, L.P. Richman, J.H. Lin, Y. H. Sun, A.J. Rech, D. Balli, C.A. Hay, Y. Sela, A.J. Merrell, S.M. Liudahl, N. Gordon, R.J. Norgard, S. Yuan, S. Yu, T. Chao, S. Ye, T.S.K. Eisinger-Mathason, R.B. Faryabi, J.W. Tobias, S.W. Lowe, L.M. Coussens, E.J. Wherry, R.H. Vonderheide, B. Z. Stanger, Tumor cell-intrinsic factors underlie heterogeneity of immune cell infiltration and response to immunotherapy, Immunity 49 (1) (2018) 178–193.e7.
[64] N. Prevarskaya, R. Skryma, Y. Shuba, Ion channels in cancer: are cancer hallmarks oncochannelopathies? Physiol. Rev. 98 (2) (2018) 559–621.
[65] I. Szabo, A. Szewczyk, Mitochondrial ion channels, Annu. Rev. Biophys. 52 (2023) 229–254.
[66] M. Bachmann, W. Li, M.J. Edwards, S.A. Ahmad, S. Patel, I. Szabo, E. Gulbins, Voltage-gated potassium channels as regulators of cell death, Front Cell Dev. Biol. 8 (2020) 611853.
[67] M. Bachmann, G. Pontarin, I. Szabo, The contribution of mitochondrial ion channels to cancer development and progression, Cell Physiol. Biochem 53 (S1) (2019) 63–78.
[68] M. Perez-Verdaguer, J. Capera, C. Serrano-Novillo, I. Estadella, D. Sastre, A. Felipe, The voltage-gated potassium channel Kv1.3 is a promising multitherapeutic target against human pathologies, Expert Opin. Ther. Targets 20 (5) (2016) 577–591.
[69] G. Panyi, C. Beeton, A. Felipe, Ion channels and anti-cancer immunity, Philos. Trans. R. Soc. Lond. B Biol. Sci. 369 (1638) (2014) 20130106.
[70] R. Eil, S.K. Vodnala, D. Clever, C.A. Klebanoff, M. Sukumar, J.H. Pan, D.C. Palmer, A. Gros, T.N. Yamamoto, S.J. Patel, G.C. Guittard, Z. Yu, V. Carbonaro, K. Okkenhaug, D.S. Schrump, W.M. Linehan, R. Roychoudhuri, N.P. Restifo, Ionic immune suppression within the tumour microenvironment limits T cell effector function, Nature 537 (7621) (2016) 539–543.
[71] A.A. Chimote, P. Hajdu, A.M. Sfyris, B.N. Gleich, T. Wise-Draper, K.A. Casper, L. Conforti, Kv1.3 channels mark functionally competent CD8+ tumor-infiltrating lymphocytes in head and neck cancer, Cancer Res 77 (1) (2017) 53–61.
[72] Z. Varga, T. Csepany, F. Papp, A. Fabian, P. Gogolak, A. Toth, G. Panyi, Potassium channel expression in human CD4+ regulatory and naïve T cells from healthy subjects and multiple sclerosis patients, Immunol. Lett. 124 (2) (2009) 95–101.
[73] A. Vallejo-Gracia, D. Sastre, M. Colomer-Molera, L. Solé, M. Navarro-Pérez, J. Capera, S.R. Roig, O. Pedrós-Gámez, I. Estadella, O. Szilágyi, G. Panyi, P. Hajdú, A. Felipe, KCNE4-dependent functional consequences of Kv1.3-related leukocyte physiology, Sci. Rep. 11 (1) (2021) 14632.
[74] R. Vicente, A. Escalada, M. Coma, G. Fuster, E. Sánchez-Tilló, C. López-Iglesias, C. Soler, C. Solsona, A. Celada, A. Felipe, Differential voltage-dependent K+ channel responses during proliferation and activation in macrophages, J. Biol. Chem. 278 (47) (2003) 46307–46320.
[75] L. Leanza, M. Zoratti, E. Gulbins, I. Szabo, Induction of apoptosis in macrophages via Kv1.3 and Kv1.5 potassium channels, Curr. Med Chem. 19 (31) (2012) 5394–5404.
[76] B. Mamnoon, J. Loganathan, M.I. Confeld, N. De Fonseka, L. Feng, J. Froberg, Y. Choi, D.M. Tuvin, V. Sathish, S. Mallik, Targeted polymeric nanoparticles for drug delivery to hypoxic, triple-negative breast tumors, ACS Appl. Bio Mater. 4 (2) (2021) 1450–1460.
[77] X. Liu, J. Jiang, Y. Ji, J. Lu, R. Chan, H. Meng, Targeted drug delivery using iRGD peptide for solid cancer treatment, Mol. Syst. Des. Eng. 2 (4) (2017) 370–379.
[78] J. Yang, J. Yang, Y. Wei, H. Yin, L. Fang, D. Chai, H. Li, H. Li, Q. Zhang, J. Zheng, Modification of IL-24 by tumor penetrating peptide iRGD enhanced its antitumor efficacy against non-small cell lung cancer, Int. Immunopharmacol. 70 (2019) 125–134.
[79] T. Singh, T. Wan Kim, ASN Murthy, M. Paul, N. Sepay, H. Jeong Kong, J. Sung Ryu, N. Rim Koo, S. Yoon, KH Song, MJ Baek, S. Jeon, J. Im, Tumor-homing peptide iRGD-conjugate enhances tumor accumulation of camptothecin for colon cancer therapy, Eur J Med Chem 265 (2024) 116050.
[80] S.M.P. Vadevoo, S. Gurung, H.S. Lee, G.R. Gunassekaran, S.M. Lee, J.W. Yoon, Y. K. Lee, B. Lee, Peptides as multifunctional players in cancer therapy, Exp. Mol. Med. 55 (6) (2023) 1099–1109.
[81] P. Cuq, A. Gross, A. Terraza, D. Fourmy, P. Clerc, J. Dornand, R. Magous, mRNAs encoding CCKB but not CCKA receptors are expressed in human T lymphocytes and Jurkat lymphoblastoid cells, Life Sci. 61 (5) (1997) 543–555.
[82] J.P. Smith, S. Wang, S. Nadella, S.A. Jablonski, L.M. Weiner, Cholecystokinin receptor antagonist alters pancreatic cancer microenvironment and increases efficacy of immune checkpoint antibody therapy in mice, Cancer Immunol. Immunother. 67 (2) (2018) 195–207.
[83] Y. Gilad, E. Noy, H. Senderowitz, A. Albeck, M.A. Firer, G. Gellerman, Dual-drug RGD conjugates provide enhanced cytotoxicity to melanoma and non-small lung cancer cells, Biopolymers 106 (2) (2016) 160–171.
[84] A. Mathieu, P. Clerc, G. Portolan, C. Bierkamp, H. Lulka, L. Pradayrol, C. Seva, D. Fourmy, M. Dufresne, Transgenic expression of CCK2 receptors sensitizes murine pancreatic acinar cells to carcinogen-induced preneoplastic lesions formation, Int J. Cancer 115 (1) (2005) 46–54.
[85] A. de Weerth, T. von Schrenck, M. Löhr, S. Mirau, H. Greten, H. Kalthoff, Human pancreatic cancer cell lines express the CCKB receptor, Hepatogastroenterology 46 (25) (1999) 472–478.
[86] P. Laverman, S. Roosenburg, M. Gotthardt, J. Park, W.J. Oyen, M. de Jong, M. R. Hellmich, F.P. Rutjes, F.L. van Delft, O.C. Boerman, Targeting of a CCK(2) receptor splice variant with (111)In-labelled cholecystokinin-8 (CCK8) and (111) In-labelled minigastrin, Eur. J. Nucl. Med Mol. Imaging 35 (2) (2008) 386–392.
[87] G.A. Clawson, T. Abraham, W. Pan, X. Tang, S.S. Linton, C.O. McGovern, W.S. Loc, J.P. Smith, P.J. Butler, M. Kester, J.H. Adair, G.L. Matters, A cholecystokinin B receptor-specific DNA aptamer for targeting pancreatic ductal adenocarcinoma, Nucleic Acid. Ther. 27 (1) (2017) 23–35.
[88] K.K. Fino, G.L. Matters, C.O. McGovern, E.L. Gilius, J.P. Smith, Downregulation of the CCK-B receptor in pancreatic cancer cells blocks proliferation and promotes apoptosis, Am. J. Physiol. Gastrointest. Liver Physiol. 302 (11) (2012) G1244–G1252.
[89] J.P. Smith, J.F. Harms, G.L. Matters, C.O. McGovern, F.M. Ruggiero, J. Liao, K. K. Fino, E.E. Ortega, E.L. Gilius, J.A. Phillips 3rd, A single nucleotide polymorphism of the cholecystokinin-B receptor predicts risk for pancreatic cancer, Cancer Biol. Ther. 13 (3) (2012) 164–174.
[90] J. Roy, K.S. Putt, D. Coppola, M.E. Leon, F.K. Khalil, B.A. Centeno, N. Clark, V. E. Stark, D.L. Morse, P.S. Low, Assessment of cholecystokinin 2 receptor (CCK2R) in neoplastic tissue, Oncotarget 7 (12) (2016) 14605–14615.
[91] A. Corlett, J.A. Pinson, M.N. Rahimi, J.V. Zuylekom, C. Cullinane, B. Blyth, P. E. Thompson, C.A. Hutton, P.D. Roselt, M.B. Haskali, Development of highly potent clinical candidates for theranostic applications against cholecystokinin-2 receptor positive cancers, J. Med. Chem. 66 (15) (2023) 10289–10303.
[92] M. Bachmann, A. Rossa, T. Varanita, B. Fioretti, L. Biasutto, S. Milenkovic, V. Checchetto, R. Peruzzo, S.A. Ahmad, S.H. Patel, R. Lukowski, M.J. Edwards, M. Ceccarelli, E. Gulbins, M. Zoratti, A. Mattarei, I. Szabo, Pharmacological targeting of the mitochondrial calcium-dependent potassium channel KCa3.1

triggers cell death and reduces tumor growth and metastasis in vivo, Cell Death Dis. 13 (12) (2022) 1055.
[93] A. Lepland, A. Malfanti, U. Haljasorg, E.K. Asciutto, M. Pickholz, M. Bringas, S. Đorđević, L. Salumäe, P. Peterson, T. Teesalu, M.J. Vicent, P. Scodeller, Depletion of mannose receptor-positive tumor-associated macrophages via a peptide-targeted star-shaped polyglutamate inhibits breast cancer progression in mice, Cancer Res. Commun. 2 (6) (2022) 533–551.
[94] Z. Tang, C. Li, B. Kang, G. Gao, C. Li, Z. Zhang, GEPIA: a web server for cancer and normal gene expression profiling and interactive analyses, Nucleic Acids Res. 45 (W1) (2017) W98–w102.